

Evidence for Asphericity in a Subluminous Type Ia Supernova: Spectropolarimetry of SN 1999by

D. Andrew Howell¹, Peter Höflich, Lifan Wang¹, and J. Craig Wheeler
 Department of Astronomy and McDonald Observatory, University of Texas at Austin,
 Austin, TX 78712
 howell, pah, lifan, wheel@astro.as.utexas.edu

ABSTRACT

We present polarization spectra near maximum light for the strongly subluminous Type Ia supernova 1999by that show that the supernova is intrinsically polarized. SN 1999by has an observed, overall level of polarization of ≈ 0.3 to 0.8% , a rise of the polarization P redward of 6500 \AA , and a change in polarization across the Si II 6150 \AA feature of about 0.4% . The presentation of the polarization at different wavelengths in the $Q - U$ plane is shown to be a powerful tool to determine the overall geometry and the interstellar component. The distribution of points with wavelength using this empirical $Q - U$ plane method reveals that SN 1999by has a well-defined axis of symmetry and suggests an interstellar polarization (ISP) vector with $P_{\text{ISP}} = 0.3\%$ and position angle $\Theta = 150^\circ$ with an error circle in the $Q - U$ plane of radius about 0.1% .

Synthetic NLTE-spectra for axisymmetric configurations based on delayed detonation models have been computed assuming ellipsoidal geometry. The input ejecta structure and composition are based on a Chandrasekhar-mass delayed-detonation model. The parameters of the explosion are chosen to reproduce the time evolution of IR-spectra of SN 1999by without further adjustments. Spherical models are then mapped onto ellipsoidal geometries and the axis ratio, viewing angle and interstellar polarization adjusted to provide the best agreement with the polarization spectra. Both flux and polarization spectra can be reasonably well reproduced by models with an asphericity of $\approx 20\%$ observed equator-on. The general properties of the polarization can be understood as a consequence of the structure of subluminous models. Best fits are obtained for the theoretical models with $P_{\text{ISP}} = 0.25\%$ and $\Theta = 140^\circ$, consistent with the empirical method.

We discuss our results for this subluminous Type Ia in the context of “normally bright” Type Ia supernovae. For normally-bright Type Ia, the photosphere

¹Present address: Institute for Nuclear and Particle Astrophysics, E. O. Lawrence Berkeley National Laboratory, Berkeley CA 94720

is near the inner iron-rich layers at maximum light and the ubiquitous iron lines give a rapid variation to the model polarization spectra. In subluminous models, the photosphere near maximum is in the silicon layers with fewer lines and a smoother overall polarization spectrum, as observed for SN 1999by. Though data are sparse, the low upper limits for polarization determined for many normal events in contrast to the high polarization in SN 1999by may suggest a relation between the asymmetry we observed and the mechanism that produces a subluminous Type Ia. Among various mechanisms, rapid rotation of the progenitor white dwarf, or an explosion during a binary white dwarf merger process are likely candidates to explain the asphericity in SN 1999by.

Subject headings: supernovae: individual (SN 1999by) — supernovae: general — polarization

1. Introduction

The last decade has witnessed the explosive growth of high-quality data on Type Ia supernovae (SNe Ia) both from the ground and from space with spectacular results and new perspectives. One of the main advances was the confirmation of the long suspected correlation between the peak brightness and the decline rate (Phillips, 1993) which clearly established that SNe Ia span a wide range in brightness but, nevertheless, most are found in a narrow range of brightness (Branch & Tammann 1992). This established SNe Ia as a tool for accurate distance determinations on cosmological scales. SNe Ia have provided new estimates for the value of the Hubble constant (H_0) based on a purely empirical procedure (Hamuy et al. 1996ab; Riess et al. 1996) and on a comparison of detailed theoretical models with observations (Höflich & Khokhlov 1996, hereafter HK96; Nugent et al. 1997). The values obtained ($H_0 \approx 65 \text{ km s}^{-1} \text{ Mpc}^{-1}$) are in good agreement with one another and with those from the HST Key Project on the Hubble Constant based on Cepheid distances. More recently, routinely successful detections of supernovae at large redshifts (Perlmutter et al. 1997, 1999; Schmidt et al. 1998; Riess et al. 1999) have provided a new tool to measure cosmological parameters such as Ω_M and Ω_Λ . This has led to refined estimates of H_0 , indicated that we live in a low matter-density Universe, and, most intriguing of all, gives hints that the cosmological constant is not zero.

Although details of the explosion are still under discussion, there is general agreement that SNe Ia result from some process of combustion of a degenerate white dwarf (Hoyle & Fowler 1960). Within this general picture, three classes of models have been considered:

(1) explosion of a CO white dwarf (WD), with mass close to the Chandrasekhar mass, which accretes mass through Roche-lobe overflow from an evolved companion star (Nomoto & Sugimoto 1977); (2) explosion of a rotating configuration formed from the merging of two low-mass WDs, caused by the loss of angular momentum due to gravitational radiation (Webbink 1984; Iben & Tutukov 1984; Paczyński 1985); and (3) explosion of a low mass CO-WD triggered by the detonation of an outer helium layer (Nomoto 1980; Woosley & Weaver 1986; HK96). Only the first two scenarios seem to be in agreement with current observations. Delayed-detonation models (Khokhlov 1991; Yamaoka et al. 1992; Woosley & Weaver 1994) of Chandrasekhar mass CO-WDs and their variations can account for the spectral and light curve evolution of “normally bright” and subluminous SNe Ia in the optical and IR (Höflich 1995a; Höflich et al. 1995a, hereafter HKW95; Wheeler et al. 1998; Lenz et al. 1999; Höflich et al. 2000). In this model, a burning front starts as a subsonic deflagration and then undergoes a transition to a supersonic detonation. Pure deflagration models like W7 (Nomoto et al. 1984) can also account for optical spectra of normal supernovae (e.g. Nugent et al. 1997). The merging scenario remains an interesting alternative which to a great extent has only been parameterized in theoretical studies but may produce results in agreement with some supernovae (HK96). The sub-Chandrasekhar model triggered by edge-lit helium ignition is disfavored on the basis of predicted light curves and spectra (Höflich et al. 1996; Nugent et al. 1997).

Despite the success of analyses of light curves and spectra, these traditional methods do not provide any direct information on the geometrical structure of the envelope. Polarization does provide information about the geometry in the scattering-dominated atmospheres of supernovae (van den Hulst 1957; Chandrasekhar 1960; Shapiro & Sutherland 1982; Höflich 1991, hereafter H91; Jeffery 1991, hereafter J91). This is because electron scattering causes the electric field vectors of scattered photons to take on a preferential orientation. For an unresolved spherical scattering atmosphere, the electric vectors cancel, yielding zero net polarization; however, in an aspherical SN, there will be increased scattering from the wings which produces electric field vectors that are not completely cancelled by scattering from the rest of the disk of the SN. In this case the observer would measure a net polarization.

Polarization can thus provide unique information on the geometry of SNe Ia that will give essential hints to understand the physics of thermonuclear explosions and the progenitor systems. Though historically the vast majority of computational models have assumed spherical symmetry, for some of the scenarios we may expect strong deviations from spherical geometry. For instance, the deflagration front has been found to be highly aspherical due to large rising plumes (Khokhlov 1995, 2000; Niemeyer & Hillebrandt 1995). For delayed detonations, the transition of the deflagration front into a detonation may occur at a point rather than in a shell (Livne 1999). The coalescence of two white dwarfs or an otherwise

rapidly rotating progenitor could also produce an overall, global asphericity. Deviations from sphericity may result in a direction dependence of the emitted flux, and consequently may affect the use of SNe Ia as distance indicators.

In this work, we report polarization measurement and interpretation of the subluminous SN 1999by. The observations are presented in §2 and the results in §3. In §4 we describe an empirical method to analyse the data and to derive the interstellar polarization. In §5, theoretical models for delayed detonations are used to analyze the observations. We close in §6 with a discussion of the results for SN 1999by, put our findings into context with other SNe Ia and different explosion scenarios, and discuss the implications for the use of SNe Ia as standard candles.

2. Observations and Data Reduction

2.1. The Imaging Grism Polarimeter

All observations were taken with the dual beam Imaging Grism Polarimeter (IGP) at the Cassegrain focus of the McDonald Observatory 2.1m telescope. IGP is the Imaging Grism Instrument (IGI) combined with spectropolarimetry optics (Goodrich 1991). IGI is a simple focal reducer with a grism that can be moved into the collimated beam. Off-the-shelf optics are used which have been anti-reflection coated for $\lambda > 4000 \text{ \AA}$. Polarization capability is provided by a modified Glan-Taylor polarizing beam splitter and a rotatable waveplate. The Glan-Taylor prism is made up of two calcite blocks. The ordinary ray (o-ray) is totally internally reflected, while the extraordinary ray (e-ray) passes through, due to different indices of refraction. The waveplate acts as a halfwave retarder and rotates the plane of polarization of incoming light. The halfwave plate is “superachromatic” with a retardance of $180^\circ \pm 2^\circ$ from 3200 \AA to 11000 \AA . The intrinsic polarization of IGP has been previously determined to be low, $P < 0.1$, see Wang, Wheeler, & Höflich (1997a; hereafter WWH97) and Wang et al. (2000a). This was confirmed with the observation of null polarization standards. More extensive information about the data reduction techniques, standard stars, and observational setup is available in Howell (2000a).

2.2. Setup of the Instrument

A $2.1''$ slit was used with the 6000 \AA grism, giving a resolution of about 14 \AA . For all observations, the 85mm lens was used in conjunction with the TK4 1024² CCD, yielding a plate scale of $0.5''$ ($\sim 3.9 \text{ \AA}$) per pixel. The spectra were wavelength calibrated with an

argon lamp. Polarization standards were observed at least once per night. The observing log is shown in Table 1.

2.3. Data Reduction

The data were reduced in IRAF, using tasks written by the authors. The reduction methods followed were those presented in Miller et al. (1988), Trammell (1994), and Howell (2000a). For SN 1999by, two sets of data were taken each night with each “set” consisting of four 20–30 minute integrations at waveplate position angles of 0, 45, 22.5, and 67.5 degrees. Polarization and flux standards were observed each night. Since spectropolarimetry measurements require a high signal-to-noise, the SN was observed over the course of three nights, and the data were combined. The data presented here have been corrected for redshift, though this correction is negligible ($z = 0.00213$).

2.4. SN 1999by

SN 1999by was discovered independently by R. Arbour, South Wonston, Hampshire, England (Arbour et al. 1999), and by the Lick Observatory Supernova Search (LOSS; cf. Treffers et al. 1997, Li et al. 1999). The SN was found on the outskirts (100'' west and 91'' north of the nucleus) of the well-known Sb galaxy NGC 2841. According to the NASA/IPAC Extragalactic Database (NED)² the host galaxy is a LINER and has a heliocentric radial velocity of 638 ± 3 km s⁻¹. According to the Lyon/Meudon Extragalactic Database (LEDA)³, the velocity corrected for Virgo infall is 811 km s⁻¹. Using $H_0 = 65$ km s⁻¹ Mpc⁻¹, this puts the distance to NGC 2841 at 12.49 Mpc, with a distance modulus of 30.48 mag. This prodigious galaxy has also produced SN 1912A (type uncertain) and the “peculiar Type I’s” SN 1957A and SN 1972R.

According to Bonanos et al. (1999), SN 1999by reached a maximum light of $B = 13.80 \pm 0.02$ on UT 1999 May 10.5, and a maximum in the V band of $V = 13.36 \pm 0.02$ (date not given). According to Weidong Li (private communication) the maxima were May 10.3 (B) and May 12.3 (V). Using a distance modulus of 30.48, and the photometry of Bonanos et al., the absolute magnitudes at peak are $M_B = -16.68$ and $M_V = -17.12$. Thus SN 1999by is underluminous by roughly 2.5 magnitudes compared to a typical SN Ia.

²<http://nedwww.ipac.caltech.edu/index.html>

³http://www-obs.univ-lyon1.fr/leda/home_leda.html

SN 1999by also had a large $\Delta m_{15}(B)$ of 1.87. This makes SN 1999by nearly as steeply declining as SN 1991bg, which had $\Delta m_{15}(B) = 1.93$. SN 1999by is thus one of the most underluminous and rapidly declining SNe Ia known. SN 1999by is similar to SN 1991bg in other respects as well. The Si II line at 5800 Å is strong relative to the line at 6150 Å, another signature of the subluminous subclass. According to Bonanos et al. (1999) the flux near 4000 Å was depressed as in other subluminous SNe Ia, a feature thought to be due to Ti II absorption. The O I feature at 7500 Å is also strong in both SN 1991bg and SN 1999by.

3. Results

3.1. Flux Spectra

Flux spectra of SN 1999by can be seen in Figure 1. Maximum light in B occurred on May 10, therefore the spectra shown are two days before, one day before, and at maximum light. Several features are apparent upon inspection Figure 1. Most obvious is the fact that SN 1999by is unquestionably a subluminous SN Ia. It is similar to the prototype, SN 1991bg.

Beginning at the blue side of the spectrum, we see that the spectrum starts near 4300 Å in a huge absorption feature. This is thought to be due to Ti II, a feature only observed in subluminous events (Filippenko et al. 1992, hereafter F92). The fact that this ionization state of Ti is seen indicates a relatively low temperature in the ejecta, since Ti II is ionized in typical SNe Ia (Nugent et al. 1995, hereafter N95). Ti II is also responsible for absorption features in the 4500–5000 Å region (F92). Moving redward, another signature of subluminous events is seen in the pair of S II lines on either side of 5400 Å. As one moves down the sequence from overluminous to subluminous SNe, the blue line is overtaken in strength by the red one (N95). Here the bluer line is scarcely seen at all, consistent with our finding that SN 1999by is a very subluminous SN Ia. From the blueshift of the absorption features of Si, one can measure an approximate velocity of this element (and thus its placement in the ejecta, since $v \propto r$). For SN 1999by we measure $v(\text{Si}) \sim 10,000 \text{ km s}^{-1}$, comparable to speeds of 10,000 and 10,600 km s^{-1} reported for SN 1991bg by F92 and Leibundgut et al. (1993), respectively. This is slightly lower than the average Si velocity in a normally bright SN Ia, 11,000 to 13,000 km s^{-1} , though velocities derived from absorption minima of broad doublets as seen in the Si II 6150 Å feature are only accurate to $\sim 1000 \text{ km s}^{-1}$.

On the far red end of the spectrum, the absorption at 7500 Å is yet another hallmark of subluminality. This line is due largely to a blend of O I $\lambda 7774$ and Mg II on the red wing, separated here by narrow atmospheric absorption. This feature is not seen in the luminous SN 1991T, but increases in strength as one goes down the luminosity sequence to

subluminous SNe Ia (N95). This O I feature is also absent in SN 1998de, a fast-declining SN Ia that was peculiar in several ways (Modjaz et al. 2000).

3.2. Polarization

The dominant sources of opacity in an SN Ia, line scattering and electron scattering, can both change the polarization of incident flux. Electron scattering polarization is independent of wavelength. In the case of axisymmetric scattering, the polarization position angle can take on only one of two values: 0° or 90° with respect to the symmetry axis (see e.g. Cropper et al. 1988; J91, H91). Line scattering need not lead to complete angular redistribution. The degree to which line scattering can polarize depends on the lower- and upper-level total angular momenta of that line (J91). Despite the fact that lines can polarize, most line scattering is less polarizing than electron scattering by an order of magnitude. As a result, electrons are the chief polarization mechanism, while the lines generally depolarize the flux previously polarized by electron scattering. Lines can redirect photons by decay in the same transition, but they can also redistribute photons to both higher and lower frequencies by further excitation or ionization from the level at which the photon is absorbed or by decay into multiple discrete lower levels (J91, Höflich 1995a).

Dust can polarize by scattering through dichroic extinction and through emission of polarized photons. Dust scattering is usually wavelength dependent, though the results vary with scattering angle. For dust typical of the ISM, the polarized flux of optical photons undergoing a single scattering can decrease with wavelength for small scattering angles, increase with wavelength for large scattering angles, or remain constant for $\Theta_{sc} \simeq 90^\circ$ (White 1979; Webb et al. 1993). Nonspherical dust grains with aligned rotation axes (from, e.g. a magnetic field) can be a source of polarization through dichroic extinction. In this case, the polarization position vector is perpendicular to the grain alignment vector.

Table 2 gives all the SNe Ia for which some polarization data are available. Figure 2 shows the normalized Stokes parameters Q and U and the flux spectrum of SN 1999by. The dashed line is the unsmoothed data. A darker colored line on the Q and U plots shows the data smoothed with a running boxcar smoothing function of 17 pixels (65 \AA). Features from $4800\text{--}5100 \text{ \AA}$ are blue, from $5100\text{--}5270 \text{ \AA}$ light blue. The S II features from 5270 to 5600 are green. The Si II features are marked by two different colors. The 5800 \AA feature is yellow, while the 6150 \AA line is magenta. Black represents the area between the Si features and the area slightly redward. Finally, the large, broad polarization feature to the red of 6500 \AA is colored red.

In Figure 3 we present $P = \sqrt{Q^2 + U^2}$ for the unsmoothed data, but we note that this indicator is biased high for low signal to noise data. Therefore, we generate the smoothed version, P_s (dark solid line) from the smoothed Q and U values. In other words,

$$P_s = \sqrt{Q_s^2 + U_s^2}, \quad [1]$$

where the subscript s denotes smoothed values. Similarly, the smoothed polarization position angle is:

$$\Theta_s = 0.5 \arctan(U_s/Q_s). \quad [2]$$

In addition to P , Figure 3 also shows Θ and the associated errors $\sigma(P)$, and $\sigma(\Theta)$.

Figure 4 shows the smoothed values for Q and U in the $Q-U$ plane for SN 1999by. The colors are identical to the color scheme used in Figure 2. In such a plot, each point defines a vector from the origin. The length of this vector is P_s and the orientation is $2\Theta_s$. Figure 4 and its implications are discussed further in §4.

As is often the case in spectropolarimetry measurements, the data for any single set of observations has a low signal to noise. Thus we have combined the data for all three nights to produce Figures 2 and 3. These figure show the sum of all observations, and consequently have the best signal to noise, with $\sigma(P) \sim 0.1\%$, and $\sigma(P_s) \sim 0.025\%$. Note that despite this low formal statistical error, systematic errors prevent us from actually discriminating small scale changes in P_s of order 0.05 to 0.1%. We use this “lowest noise” case for most subsequent analysis, but we also look to the individual data sets for confirmation that features are real. Figure 5 shows the results of combining the data in different ways. The top panel shows P derived from all observations. The second panel shows P constructed from only the best four data sets. The third panel shows P from the best single data set, taken on May 10 when the supernova was at maximum light. Finally, the lower panel of Figure 5 shows the sum of the best data from May 8 and 9 combined with the second best data set from May 10. These are the next three best data sets after the best set from May 10. The dashed lines in Figure 5 are 1σ errors. Our indicator P_s falls beneath the midpoint of the unsmoothed data because P is biased high as an indicator, though P_s is less biased. The degree of the bias to P increases with low signal to noise data. We also tested Wang’s indicator, (WWH97) and the rotated Stokes parameter (e.g. Tran 1995), and both agree with P_s to within 0.02% across all wavelengths. It is important to remember that there is no perfect indicator for the total degree of polarization (Leonard et al. 2000b; Simmons & Stewart 1985). Three features stand out in every data set. These are: the overall level of $P \sim 0.25\%$, the change in Θ across the 6150 Å Si II feature, and the rise in P to 0.6% at 6900 Å. We discuss each in turn.

The Level of P : The first of these significant features is that throughout most of the

spectrum $P \sim 0.25\%$, with some excursions to lower values. Not every bump in the smoothed data in Figure 5 is significant because smoothing can introduce artifacts into low signal to noise data; however, the overall level of $P_s \simeq 0.25\%$ shown in Figure 3 is significant. The statistical error for P is $\sigma(p) \sim 0.1\%$ in the region of interest, and the statistical error for the smoothed spectrum is $\sigma(P_s) \sim 0.025\%$. We should also keep in mind that the fact that we have smoothed the data means that we cannot distinguish features narrower than 65 \AA .

Si II 6150 \AA : An overall level of polarization is interesting, but could be caused by interstellar or circumstellar sources. Perhaps the most striking feature of the spectropolarimetry of SN 1999by is then the change in position angle, Θ , of the polarization through the Si II 6150 \AA feature as seen in Figure 3. The PA jumps from 100° to 150° over this region, peaking at 6200 \AA . As shown in the second panel of Figure 3, $\sigma(\Theta) \sim 12^\circ$ without smoothing. After smoothing, $\sigma(\Theta) \sim 3^\circ$. *Even without smoothing, the change in Θ across Si is a 4σ result.* This is clear evidence that the SN is intrinsically polarized.

It is also remarkable that the polarization change in Si is roughly equal to the polarization change across the entire wavelength region. At 4800 \AA $\Theta \simeq 150^\circ$ but, by 7100 \AA Θ has dropped to $\simeq 90^\circ$. This is significant because we will later show that there is a single choice of interstellar polarization that, when subtracted from the data, reduces the position angle across all wavelengths to nearly a single value.

The 6900 \AA Rise: The rise in polarization toward the red peaks at $P \sim 0.6\%$ at 6900 \AA . This feature is wider (1000 \AA) than any particular line, and it occurs in a region normally blanketed by Fe-peak lines. Such a rise in polarization in this wavelength region was predicted theoretically by WWH97. We will revisit this feature when we discuss the theoretical interpretation of the data in §5.

4. Data Analysis Using the $Q - U$ Plane

The $Q - U$ plane is a powerful tool for interpreting SN polarimetry data both with respect to testing the overall geometry and to determining the interstellar component of the polarization.

4.1. Intrinsic Properties of SN 1999by

The $Q - U$ plot for the smoothed data of SN 1999by is given in Figure 4. Each point corresponds to one pixel. The points are color coded to reflect their distribution in wavelength. The color coding is from Figure 2 which shows the smoothed Q , U , and flux spectra.

Polarization arising from axisymmetric scattering will show up as a straight line on the $Q-U$ plot (see e.g. Cropper et al. 1988; J91). Uncorrected for interstellar polarization, the data for SN 1999by clearly define an axis of symmetry in Figure 4. The scatter is $\approx 0.1\%$, comparable to the scatter expected from photon statistics and systematic effects.

The distribution of the Si II 6150 Å feature is particularly interesting, as noted in the previous section. Here the Si feature is colored magenta. It was previously noted that the variation in position angle across the Si feature matches the variation in position angle seen across the entire wavelength region of study. Stated another way, Si II is not localized to one spot on the $Q-U$ diagram, but is distributed throughout the “line” demarked by the rest of the points in the plot, except the points from the 6900 Å region, which are colored red. Physically, this means that Si does not have a special geometry — it shares the same axis of symmetry as the rest of the SN.

There is a slight deviation from linearity in the red points on Figure 4. If we take this jog to be real, noting that it is nearly perpendicular to the rest of the points, then the jog corresponds to a switching from an oblate to a prolate geometry in the corresponding wavelength region or vice versa. This seems to be an unnecessary complication of the model. The discrepant points can be explained by noise. If a point deviates from the line by 3σ , smoothing can introduce correlated errors, causing several neighboring points to appear to deviate from the line as well. On the basis of these few points, it is not possible to conclude that there are deviations from the global geometry in this wavelength region.

4.2. Interstellar Polarization

Interstellar Polarization (ISP) due to dust in the interstellar medium of both the host galaxy and the Milky Way can change the observed polarization spectrum of an object. The difficult question of how much of the polarization signature measured for SN 1999by is intrinsic and how much is interstellar plagues polarization measurements of all objects. The issue is particularly difficult in the case of extragalactic objects which can have two sources of ISP — one contribution from our Galaxy, and one from the host galaxy. Fortunately, we can estimate the ISP for SN 1999by via two essentially independent methods, the empirical $Q-U$ plane method and theoretical considerations. We will discuss these specific techniques below, but in this section we provide general constraints on interstellar polarization.

The maximum interstellar polarization allowable, corresponding to the most favorable alignment of dust grains along the line of sight is $9\% \times E(B-V)$ (Serkowski, Mathewson & Ford 1975). The galactic longitude of SN 1999by is 166.91° and latitude 44.12° (NED). The

Galactic extinction towards NGC 2841 is estimated to be $A_B = 0.070$ mag (Schlegel et al. 1998) though Burstein & Heiles (1982) give $A_B = 0.000$ mag. Schlegel et al. also estimate $E(B - V) = 0.016$ mag. Using Schlegel’s estimate of $E(B - V) = 0.016$ mag, the maximum Galactic component of polarization is 0.144%. This is indicated by a dashed circle in the $Q - U$ plane diagram of Figure 4.

Some limited information about the Galactic component of ISP can be gleaned from observations of stars near the line of sight to SN 1999by. There are only three stars with polarization measurements in the literature within $\pm 5^\circ$ of SN 1999by, and they are presented in Table 3. They are also plotted as light blue asterisks on the $Q - U$ plane, Figure 4. The closest star to SN 1999by is HD 82328. It is 2.16° away from the SN on the sky. While HD 82328 shows a low level of polarization, $P = 0.01\%$, it is also the closest star at 19 pc, so it does not sample much of the ISP between us and the supernova. The next closest star, HD 82621 is 2.7° away with $P = 0.05\%$, but it is only 40 pc away. If we go out to HD 77770, we can look through 1.3 kpc of the Galaxy to see $P = 0.37\%$, but now we are looking 3.25° away from the line of sight to the SN. This is probably the reason this star is outside the allowed Galactic ISP region of Figure 4. The three stars also have different polarization position angles, and it is likely that any Galactic polarization toward SN 1999by would have still a different position angle. In addition, if there is a contribution from ISP in the spectrum of SN 1999by, it could arise from the host galaxy. These three stars alone do not allow us to place meaningful limits on the ISP. Fortunately, the $Q - U$ plane does suggest a choice of interstellar polarization.

4.3. ISP Subtraction

ISP is a smoothly varying function of wavelength, described by the Serkowski law:

$$P/P_{\max} = \exp[-K \ln^2(\lambda_{\max}/\lambda)]$$

where p is the percent polarization at wavelength λ , P_{\max} is the maximum polarization at wavelength λ_{\max} and $K = 0.01 + 1.66\lambda_{\max}$, (λ is in microns; Whittet et al. 1992).

To remove ISP, we subtract a Serkowski law from the data. This is essentially a vector subtraction in the $Q - U$ plane. Correcting for interstellar polarization can either increase or decrease the derived intrinsic polarization of the object, and it can turn absorption features into emission features and vice versa. This is easy to understand if we remember that we are “undiluting” the light from the SN by removing contaminating ISP. Mathematically, this is because the combination of the intrinsic polarization and ISP is a vector addition.

To remove the interstellar signature from our data, we must first determine P_{ISP} . As

remarked above, the data points fall on a line in the $Q-U$ plane of Figure 4. We can assume for SNe Ia that some parts of the spectra are depolarized (WWH97). Taken together, this allows two possible choices of interstellar polarization (see Wang et al. 2000b). If we place the ISP at either end of the line delineated by the data points and subtract it, then the data will fall along a radial line in $Q-U$ space with essentially one constant value of Θ for the system (note that Θ is one-half the angle of a vector on the $Q-U$ plane). It is unlikely that the ISP point could be placed well within the spread of unsubtracted SN 1999by points. In this case, after subtraction the position angle would change abruptly where there was no particular feature in the polarization spectrum. We argue that this behavior is not likely to be physical.

The two choices for ISP are the light blue circles marked as A and B in Figure 4. The diameter of the circles corresponds to the approximate uncertainty in the placement of the ISP. ISP A has a value of $P = 0.65\%$ and $\Theta = 82.5^\circ$. ISP B has a value of $P = 0.3\%$ and $\Theta = 150^\circ$. Both of the choices for interstellar polarization lie outside of that allowed for the Galaxy along the line of sight to SN 1999by. Assuming that the $E(B-V)$ of Schegel et al. (1998) is correct, this implies that some of the ISP arose in the host galaxy. Note that we could place the ISP any place on the line defined by the data in the $Q-U$ plane that was not well within the spread of data points. The further the ISP from the data, the more tightly, but arbitrarily, the ISP position angle would be defined. We cannot rule out more extreme choices, but argue that the ISP is most plausibly at either A or B so that some portions of the data represent low polarization in the supernova. We think this argument applies to SNe Ia, but note that the data on the Type II SN 1999em show that at some phases there is finite polarization at all observed wavelengths (Wang et al. 2000b).

ISP Choice A: First we consider ISP A. Figure 6 presents the resulting Q , U , P , and Θ with this choice of P_{ISP} subtracted from the data. Note that in the lower panel, the effect of removing the interstellar polarization is that the position angle becomes nearly constant across the entire wavelength region. There is some deviation at longer wavelengths. This is due to the fact that when the ISP-corrected points are relocated on the $Q-U$ plane, the long wavelength points are closest to the origin, and deviations in position angle are magnified. ISP A is disfavored for three reasons: it produces a decrease in polarization at 7000 \AA , it produces an increase in polarization in the Si II 6150 \AA feature, and it is less likely due to reddening considerations. We consider each in turn.

Subtracting ISP A produces a high $P \sim 0.8\%$, at short wavelengths, and a decrease in polarization at wavelengths greater than 6500 \AA . This is contrary to theoretical expectations. Numerical calculations presented in WWH97 predicted a *rise* in polarization longward of 6500 \AA due to decreased line blanketing. This is discussed in further detail below in §5.

The removal of ISP A from the data also causes the polarization to be enhanced in the Si 6150 Å feature. While this increase cannot be ruled out completely, from a theoretical perspective, this feature is easier to understand if it is a depolarization. P-Cygni lines are generated above the photosphere, so polarization produced by electron scattering at the photosphere is expected to be depolarized by absorption and reemission in the layers above it (see the appendix). Note that by using this qualitative theoretical prediction to discriminate between the two choices of ISP, the “empirical method” is not completely independent of theory. However, the approach is significantly different from the determination of ISP from a quantitative comparison to a specific theoretical model as done in §5 below.

Another consideration that slightly disfavors the choice of ISP A is the observational constraint that the SN does not appear to be reddened. As mentioned above, the maximum interstellar polarization allowable, corresponding to the most favorable alignment of dust grains along the line of sight is $9\% \times E(B - V)$. We can use this to place a lower limit on the reddening expected from our choice of ISP. Inverting, we have:

$$E(B - V) \geq P_{\text{ISP}}/9\% \quad [4]$$

Thus for model A, $E(B - V) \geq 0.072$, and for a standard extinction law (Savage & Mathis 1979), $A_V \geq 0.22$. Given that SN 1999by is already bluer than SN 1991bg, which was thought to have low extinction along the line of sight, it is likely that SN 1999by is not significantly reddened. SN 1999by has a pseudocolor of $B_{\text{max}} - V_{\text{max}} = 0.44 - 0.47$ (Bonnanos 1999; Li, private communication). This compares to a value of $(B - V)_{\text{max}} = 0.74$ for SN 1991bg (M97). Note that $B_{\text{max}} - V_{\text{max}}$ and $(B - V)_{\text{max}} = 0.74$ are not, strictly speaking, the same quantity, but this is the closest comparison we can make until the photometry data is published. Both SN 1991bg and SN 1999by are redder than typical SNe Ia, but this is thought to be intrinsic to subluminous SNe Ia (F92; Leibundgut et al. 1993; HKW95; Turatto et al. 1996; Mazzali et al. 1997). Since neither the extinction towards SN 1991bg nor towards SN 1999by is known with certainty, and we can only place a lower limit on the reddening expected from our model, this is not a hard limit.

ISP Choice B: The subtraction of ISP B from the data, like ISP A, causes the SN data to lie essentially on a straight radial line in the $Q - U$ plane as can be seen in Figure 7. For this choice of ISP, the polarization deduced for the SN has a constant position angle of $\Theta \simeq 80^\circ$ across the entire wavelength region. In the bottom panel of Figure 8, the ISP subtracted data is compared to the position angle from the non-ISP-corrected data. This figure also shows smoothed and unsmoothed versions of P , Q , and U after ISP correction. ISP B is slightly favored due to reddening considerations. For this model $E(B - V) \geq 0.033$, and $A_V \geq 0.10$, less than half that of ISP A. From a theoretical perspective, this choice also gives the desired depolarization of the Si feature. ISP B also gives a rise in polarization at

red wavelengths as theoretically predicted. For these reasons it is a better choice than ISP A.

With ISP B subtracted, we find $P \sim 0.4\%$ from 5600 – 6600 Å with the exception of the Si feature. The difference between the polarization maximum at 6900 Å and the overall level, (e.g. at 5800 Å), is 0.4%. This relative difference does not depend on the choice of ISP given the assumption that intrinsic polarization defines a radial line on the $Q - U$ plot. The maximum degree of polarization after subtraction of ISP B is $P = 0.8\%$. As noted above, subtraction of ISP A gives the same maximum value, but for ISP B the maximum polarization occurs at wavelengths ≥ 6500 Å. This is where the maximum polarization is expected from theory (WWH97). The subtraction of ISP B produces relative depolarization around 4800–5600 Å, where the level is 0.2% or lower. This is where line blanketing opacity dominates electron scattering opacity and thus is where depolarization is expected from theory (Höflich, Müller & Khokhlov 1993, hereafter HMK93; WWH97).

We have estimated the degree of uncertainty associated with this choice of ISP by choosing different values of P_{ISP} close to ISP B and observing the degree to which they cause the axis ratio of the system to deviate from a single value across all wavelengths. These are shown in Howell (2000a), but are omitted here for brevity. After consideration of the uncertainties, our best choice of ISP, Case B, is $P = 0.3 \pm 0.05\%$ at $\Theta = 150 \pm 5^\circ$.

Regardless of whether we choose ISP A or B, the intrinsic polarization of SN 1999by, given by the total length of the distribution of points in the $Q - U$ plane, is $P = 0.8\%$. As mentioned earlier, Si is distributed throughout most of the line in the $Q - U$ plane and hence samples this total intrinsic polarization. One implication is that the Si 6150 Å feature will always show a minimum or maximum in the polarization after subtraction of a reasonable choice of ISP lying at one or the other extreme of the data in the $Q - U$ plane.

5. Comparison with Theoretical Models

The chemical and density structures for the initial models are based on calculations of the stellar evolution from the main sequence to white dwarf formation and the subsequent phase of accretion onto the white dwarf (Umeda et al. 1999; Höflich, et al. 2000). Spherical dynamical explosions and corresponding light curves are first calculated. Aspherical structures are then constructed by mapping the spherical structures in the homologous expansion phase onto ellipsoidal density structures with an axis ratio a/b . Here a is the equatorial major axis and b is the polar major axis. Subsequently, detailed non-LTE spectra are calculated for the flux and polarization. Details are given in the appendix.

Delayed detonation (DD) models and pulsating delayed detonation models have been found to reproduce the optical and infrared light curves and spectra of SNe Ia reasonably well (Höflich 1995b; HKW95; HK96; Nugent et al. 1997; Wheeler et al. 1998; Lenz et al. 1999; Höflich et al. 2000; Gerardy et al. 2000). In particular, the DD models with a variation in the parameter, ρ_{tr} , at which the transition is made from deflagration to detonation, give a range of ejecta structures and mass of ^{56}Ni . Models with smaller transition density give less nickel and hence both lower peak luminosity and lower temperatures. The latter gives lower opacities and hence a steeper decline in the light curve. The DD models thus give a natural and physically well-motivated origin of the brightness-decline rate relation of SNe Ia within the paradigm of thermonuclear combustion of Chandrasekhar-mass CO white dwarfs (HKW95; Höflich et al. 1996).

Here we present the polarization spectra of a DD model with parameters which have been adjusted to provide a fit to the time evolution of the infrared spectra observed for SN 1999by (Gerardy et al. 2000) without further tuning. In the delayed detonation scenario, the transition density, ρ_{tr} , is the dominant factor that determines the amount of ^{56}Ni produced and hence distinguishes the normally-bright from the subluminous models (HKW95; Höflich 1995a; Iwamoto et al. 1999). We contrast the ejecta structure of a normally-bright SN Ia model with that required to reproduce a subluminous event like SN 1999by in Figure 9. The same progenitor structure and central density at the time of the explosion have been taken as the normally-bright SNe Ia studied in Höflich et al. (2000). We assume a WD with a Chandrasekhar mass and solar metallicity which originates from a main sequence star of $7 M_{\odot}$ (Umeda et al. 1999). At the time of the explosion, the central density is $\rho_c = 2 \times 10^9 \text{ g cm}^{-3}$. To produce a subluminous supernova consistent with the IR-spectra of SN 1999by, ρ_{tr} has been chosen to be $1 \times 10^7 \text{ g cm}^{-3}$ compared to $\rho_{tr} = 2.5 \times 10^7 \text{ g cm}^{-3}$ for the normally-bright model. The subluminous model produced $0.103 M_{\odot}$ of ^{56}Ni compared to $0.701 M_{\odot}$ for the normally-bright model. A typical feature of subluminous DD models is the greater production of O, S and Si (0.251 , 0.431 and $0.221 M_{\odot}$, respectively) compared to normally-bright SNe Ia (0.065 , 0.215 and $0.123 M_{\odot}$, respectively). Another feature of subluminous SNe Ia models is that the ^{56}Ni is constrained to the inner layers with low expansion velocities which become visible a few weeks after maximum light. In contrast, for normally-bright SNe Ia models, the outer edge of the ^{56}Ni layers extends to about $10,000$ to $13,000 \text{ km s}^{-1}$ so that the Ni is already visible at maximum light (Figure 9). As we will see below, this qualitative difference between normally-bright and subluminous SNe Ia has important implications for our understanding of the polarization spectra. For more details on the explosion models, light curves and spectral evolution, see Höflich et al. 2000 and Gerardy et al. (2000).

For this paper, we calculated the polarization spectrum at day 15 after the explosion

which corresponds to maximum light in B. At this epoch the model gives $M_V = -17.52^m$, and $B - V = +0.46$. The temperature structures for the aspherical models were based on the spherical calculations. The optical spectrum is formed in layers with expansion velocities between ≈ 8000 and $14,000 \text{ km s}^{-1}$ which corresponds to about $1 M_\odot$ in mass coordinate, i. e. in layers dominated by intermediate mass elements (Figure 9). We calculated the spectra for a variety of ellipsoidal structures at the photosphere with axis ratios a/b between 1.15 and 1.5 and adjusted a/b to fit the level of polarization observed in SN 1999by for various inclination angles.

Currently, three-dimensional models are not a suitable tool to adjust parameters such as the main sequence mass, accretion rates, metallicity, rotation and combustion physics to find best fits. Therefore, we restrict our discussion of the fluxes to the main spectral features.

In our model, the spectrum at day 15 is formed at the outer edge of the Si-rich layers, i.e. well above the region containing ^{56}Ni (Figure 9). The top panel of Figure 10 shows reasonable agreement between theoretical and observed features, and thus confirms the validity of this model in terms of Doppler shifts of the lines, their strengths, the ionization stages, and the overall slope of the spectrum. Most of the strong features can be attributed to the intermediate mass elements O I, S II and Si II. Most of the weaker lines are due to iron-group elements which are singly ionized as expected for subluminous SNe Ia with a relatively cool photosphere (Höflich et al. 1995b). The O I feature at about 7450 \AA is too weak in the models. This is not due to a lack of oxygen (Figure 9), but the strength of the O I line depends sensitively on the excitation. The discrepancy may be an artifact of the approximations imposed by the numerical treatment, or it may hint at the need for a slightly higher excitation in the outer layers, e. g. due to non-thermal electrons or an increased γ -ray flux. We note that some fast-declining (subluminous) SNe Ia do not show strong O I in their spectra (Modjaz et al. 2000).

The flux spectrum depends on the inclination, i (here taken to be the angle between the equatorial plane and the line of sight). For oblate geometries, the flux increases with i because of the increased escape probability of photons towards polar directions (H91). Although the asphericity is small in our example, the absolute flux varies by about 30% or 0.3^m from equator to pole. With increasing i , weak absorption features (e.g. due to Fe II, S II) tend to be smeared out, and the overall spectrum becomes smoother as shown in the top panel of Figure 10. These absorption features are formed in a narrow region close to the origin of the quasi-continuum which is produced by electron scattering, bound-free processes, and by a large number of very weak lines (Höflich 1995a). Because $v \propto r$, for an oblate geometry the photosphere seen by an observer spans a wider velocity range as i increases. In addition, the probability of multiple scattering of photons tangential to the

photosphere into the “absorption” feature increases with i in the case of oblate geometries, thus diluting the depolarization of the line.

Flux and polarization spectra of a model with 17% asymmetry observed at various inclination angles are shown in Figure 10 in comparison with observations. The model polarization spectra have been rebinned with $\Delta\lambda = 12.5\text{\AA}$, to provide a statistical error comparable to the observations which, for this section, have been rebinned with $\Delta\lambda = 45\text{\AA}$. The model polarization spectra for various choices of the inclination, i , and the raw and binned data are given in the second panel of Figure 10. The statistical errors in the model and observations and the polarization angle before and after correcting for the model-determined ISP are given in the third and fourth panels of Figure 10, respectively.

In the models, the polarization is produced by electron scattering. As discussed in the appendix, we assume complete redistribution for lines which causes depolarization in lines. As expected both from analytical and numerical studies, the polarization $P \propto \cos^2 i$ (e.g. van den Hulst 1957; H91). The frequency dependence of the polarization is governed by the absorption probability in lines relative to electron scattering. Most prominent is the strong depolarization by the Si II line at 6150\AA and the O I, Mg II and Si II features at 7600\AA (Figure 10, panel 2). At shorter wavelengths, a large number of overlapping lines due to iron-group elements is responsible for the low polarization. The wavelength region above 5400\AA shows an increasing degree of polarization due to the decreasing importance of line opacities. Shortwards of the Si II line at 6150\AA , the polarization level in the models is generally lower and shows modulations due to moderately strong Si II, S II, and Fe II lines, as expected from the opacity pattern for Si-rich layers at temperatures between 5000 to 10000 K (see Figure 1 in HMK93).

We note that the frequency pattern of the model polarization spectra for subluminous supernovae is rather different from normally-bright SNe Ia at the same phase (e.g. SN 1996X, WWH97). In the latter, the polarization spectra near maximum light are dominated by iron-group elements because the photosphere is between 10,000 and 12,000 km s^{-1} , i. e. right at the interface between complete and incomplete Si burning (Figure 9). In addition, the photospheric temperatures are higher than in subluminous events by several thousand degrees and, thus, iron-group elements are present both in the second and third ionization stage. The presence of these ubiquitous iron lines gives a more pronounced rapid frequency dependence of the model polarization spectra for the normally-bright SNe Ia near maximum as contrasted with the relatively smooth variation predicted for the polarization spectra of the subluminous events.

We have iterated the component of the interstellar polarization to optimize the fits with respect to the line width and depth of the strong lines, in particular the Si II feature

at 6150 Å. The best agreement is for $P_{\text{ISP}} = 0.25\%$ and $\Theta = 140^\circ$. Small changes of the ISP-vector result in slightly broader components of the depolarization features. With increasing deviations from the optimized values, local maxima appear in the line centers which eventually dominate the spectra. The vector for the interstellar polarization derived in this way is consistent with the contribution of the ISP found with the empirical method described in §4.3. The agreement supports the soundness and reliability of both the empirical and theoretical approaches.

As shown in Figure 10 (panel 2), the observed polarization spectrum can be reproduced by an ellipsoid with an axis ratio of 1.17 seen equator on ($i \approx 0^\circ$). The overall level of polarization in different wavelength ranges and the velocity shift and strength of features produced by strong lines are consistent.

The theoretical polarization spectrum shows a distinct physical pattern between 5400 and 6000 Å at the 0.1% level which cannot be discriminated in the data. These small scale fluctuations may be valuable tools to analyze small scale structures caused by inhomogeneous mixing if better data become available in the future.

An axis ratio of 1.17 is a lower limit to the amount of asphericity that is required, though we can also estimate an upper limit. As an alternative to a model with small asphericity seen equator on, models with larger asphericity may be able to reproduce the observations if seen from larger inclinations, i . To test this possibility, we have calculated a set of models with larger axis ratios as presented in Figure 11. To reproduce the overall level of polarization for i of 28° and 52° , the axis ratio a/b must be boosted to 1.25 and 1.5, respectively. Strong discrepancies at the 0.3%-level are present for $i = 52^\circ$ which are well beyond the level of uncertainty. Most noticeable are the strong peaks in P at about 6000 and 6400 Å, and the change of 0.6% between 5800 and 6000 Å. Such variations cannot be eliminated by a different choice for ISP. For $i = 28^\circ$ and $a/b=1.25$, the agreement with the observation of P is better, but problems remain on the level of 0.2%, and there are some problems with the location of the Si II minima. The model with $i = 28^\circ$ may be marginally consistent with the observations. We can conclude that SN 1999by has intrinsic asymmetries of the order of $\approx 20\%$ and that it is seen almost equator on.

6. Discussion and Conclusions

Whereas core collapse supernovae are commonly found to be polarized at 1% or greater, the degree of polarization is much smaller in SNe Ia (Wang et al. 1996, 2000a). Spectropolarimetric and broadband measurements of polarization in SNe Ia are still exceedingly rare.

For most measurements, the interstellar component cannot be determined, making any intrinsic component impossible to determine. Table 2 shows all SNe Ia for which polarization data are available. McCall et al. (1984b) measured no significant polarization intrinsic to SN 1983G, but did place (large) upper limits on spectropolarimetric signatures. The first slightly subluminal SN Ia with a polarization measurement was SN 1986G. Broadband UBVRIJH polarimetry with a maximum polarization of 5.2% is well fit by a Serkowski law (Hough et al. 1987). Broadband polarimetry of SN 1998bu is presented in Hernandez et al. (2000). The polarization, ranging from 1–2% again follows the Serkowski law. Spyromilio & Bailey (1993) placed limits on the spectropolarimetry of SN 1992A which was observed about 15 days and 100 days past maximum light. The overall level of P is roughly 0.3%, comparable to the noise level. While Spyromilio & Bailey make no claim for intrinsic polarization of the SN, polarization signatures of the type suggested for SN 1996X (WWH97) cannot be ruled out from the published data. Leonard et al. (2000a) presented spectropolarimetry of SN 1997dt, showing apparent changes in P across spectral features. The level of intrinsic versus interstellar polarization is not known.

WWH97 observed the normally-bright supernova SN 1996X about one week before maximum light in V. The data showed a small average polarization with modulations on the level of 0.2%. WWH97 concluded that SN 1996X could have only a very small, if any, global asymmetry in the geometry, given the lack of detectable mean polarization, but that the modulations were consistent with inhomogeneities in distributions of the elements within the ejecta. Figure 12 shows the data for SN 1996X and SN 1999by in the $Q - U$ plane. The lack of any preferred orientation to the data and hence a global asymmetry for SN 1996X contrasts distinctly with the linear distribution of points for SN 1999by. The finer scale variations in the polarization spectra of SN 1996X are qualitatively similar to the expectations for the behavior of a photosphere significantly contaminated with iron-peak elements as a normally-bright SN Ia should be (Figure 9, WWH97). A comparison with detailed model calculations for a delayed detonation model confirmed that the data are consistent with little or no global asymmetry in the density structure of SN 1996X. The continuum polarization in the model is modulated by ubiquitous weak lines of Fe II-III, Co II-III and Ni II-III that serve to depolarize on scales of $\approx 100 \text{ \AA}$. These lines are formed at the interface region between complete and incomplete Si burning. WWH97 suggest that there is an asymmetry in the *chemical* structure that may be a relict of the chemical plumes rising during the deflagration phase. Strong depolarization over the Si II 6150 \AA feature is predicted by the model, but not observed. As noted in WWH97, another problem with the comparison to theory of SN 1996X is that the model shows a rise in the polarization longward of 6500 \AA which is not apparent in the data. SN 1999by shows both the depolarization at the Si II feature and the rise in the polarization level to the red.

One of the open questions in SNe Ia research is the nature of the very subluminoous subclass. The prototypical example of this subclass is SN 1991bg. Light curves and spectra of SN 1991bg are presented in F92, Leibundgut et al. (1993), and Turatto et al. (1996). Other subluminoous SNe include SN 1992K (Hamuy et al. 1994), SN 1997cn (Turatto et al. 1998) and SN 1998de (Modjaz et al. 2000). Subluminoous SNe Ia may be rare, but some analyses indicate that they could make up 16% (Li et al. 2000) or more (Schaefer 1996) of all local SNe Ia. Some defining characteristics of the subclass are rapidly-declining light curves ($\Delta m_{15}(B) \simeq 1.9$), fainter than normal peak magnitudes by 2–3 mag, redder colors at maximum ($(B - V)_{\max} \simeq 0.4\text{--}0.74$), a non-existent or weak secondary maximum in R and I, and an earlier transition to the nebular phase. Moreover, the ^{56}Ni region is limited to expansion velocities below 4000 to 4500 km s $^{-1}$, i.e. about a factor of 2 to 3 times smaller than in normally-bright SNe Ia. By comparison, the expansion velocity implied by Si II indicates a wider range of the Si-dominated layers in subluminoous SNe Ia (≈ 5000 to 12,000 km s $^{-1}$) compared to normally-bright SNe Ia (≈ 9000 to 13,000 km s $^{-1}$; Turatto et al. 1996; Gerardy et al. 2000). Subluminoous events also show strong absorption features at 4200 Å (Ti II), 5800 Å (Si II), 7500 Å (O I & Mg II) and 8300 Å (Ca II). Theoretical interpretations of subluminoous SNe Ia given in Ruiz-Lapuente et al. (1993), Woosley & Weaver (1994), HKW95, N95, Mazzali et al. (1997), and Milne et al. (1999) include all three types of explosion mechanisms outlined in §1.

SN 1999by is the first subluminoous SN Ia to show definitive evidence for intrinsic polarization. Before ISP correction, the supernova shows an overall level of polarization, a rise in P redward of 6500 Å, and a change in polarization position angle across the Si II 6150 Å feature. The strong wavelength dependence and the individual features are not expected from interstellar polarization and show the need for a component intrinsic to the supernova.

We employ a new method (see Wang et al. 2000b) for the analyses the polarization data of supernovae by using the $Q - U$ plane. This representation provides important constraints on the overall geometry of the configuration, and it allows strong constraints to be placed on the ISP if the data points are aligned. The small spread of the data points in SN 1999by about a line in the $Q - U$ plane reveals that the SN has a well-defined axis of symmetry. Though the spread around this line is consistent with rotational symmetry, we cannot exclude small additional off-axis components. In the classical approach to determine the polarization component of the ISM, the object needs to be observed at several epochs from which the polarization vector can be deduced by the reasonable assumption that it is time invariant. In the $Q - U$ plane and for reasonable assumptions for the polarization mechanism, we have shown that the component of the ISM can be determined by the vector between the origin of the $Q - U$ plane and the endpoint of the line of the polarization data points. Obviously, with this choice, the polarization position angle should not vary over lines. The residuals can

be used to judge the quality of the data and the assumptions. For SN 1999by, this method suggests that the $P_{\text{ISP}} = 0.3\%$ with $\Theta = 150^\circ$ which is consistent with the best fits for the ISM based on detailed models ($P_{\text{ISP}} = 0.25\%$, $\Theta = 140^\circ$).

Based on a delayed detonation model, synthetic NLTE-spectra have been computed and compared to the observations. The free parameters have been adopted from a spherical delayed detonation model that reproduces the infrared spectrum of SN 1999by between 1 and 2 μm and its evolution with time (Gerardy et al. 2000). No further tuning of the initial model is done to fit the polarization data, although three new parameters must be introduced, the axis ratio, the angle of the line of sight to an observer, and the ISP. The ISP could be taken from the observations, but the theoretical analysis independently confirms the empirical value. The axis ratio and inclination angle are constrained by two aspects of the observations: the overall level of polarization and the shapes of spectral features. The initial spherical model is remapped to an ellipsoidal geometry with an axis ratio of a/b . The axis ratio a/b has been adjusted to provide the overall level of P observed. Both the optical flux spectra and polarization spectra of SN 1999by can be reproduced by models with an asphericity of $\approx 20\%$ which is seen equator on. Higher inclinations, which require larger axis ratios to give the overall polarization, can be ruled out from the spurious frequency dependence of the resulting polarization spectra.

The relatively high polarization we observe for SN 1999by may be a significant clue to the nature of SNe Ia. Existing limits on polarization of other SNe Ia are very sparse (7 objects at the time of this paper, see Table 2). The polarization due to asphericity decreases with inclination, further reducing the significance of any statistics. Within these limitations, we would have expected to see more polarized SNe Ia if $P \approx 0.6$ to 0.8% is common. The lack of such detections supports the notion that the intrinsic polarization of the subluminous SN 1999by is unusually large. Another argument is that, although small, the size of the asymmetry we derive implies a change of the observed luminosity of about 0.3^m from equator to pole. This spread is larger by a factor of ≈ 1.5 than the mean dispersion in the brightness-decline relation $M(\Delta m_{15}(B))$ (Hamuy et al. 1995; Riess et al. 1999). The dispersion in $M(\Delta m_{15}(B))$ is dominated by the normally-bright SNe Ia and the orientation of the symmetry axis of a given supernova is arbitrary. Taken together, these facts again suggest that the asphericity is unusually large for SN 1999by compared to most normally-bright SNe Ia. The low mean polarization observed for the normal SN 1996X (WWH97) is consistent with this. If future observations confirm that the large asphericity of SN 1999by is characteristic of subluminous SNe Ia, this may provide important clues to the physical reasons for both normal and less-than-normal peak luminosity.

Our quantitative analysis of the data of SN 1999by was based on delayed-detonation

models with imposed asphericity without addressing the question of the physical mechanism which produces aspherical envelopes. Within the delayed detonation model, possible mechanisms to induce asymmetry include the following: 1) instabilities in the nuclear burning front during the deflagration phase, 2) rapid rotation of the progenitor white dwarf, 3) delayed detonation transition at a point rather than simultaneously on a sphere, and 4) impact of the supernova ejecta on the secondary star. Aspherical configurations may also be the result of 5) the merging process of two degenerate white dwarfs and 6), in principle, edge-lit helium detonations in sub-Chandrasekhar mass WDs.

Studies of the deflagration phase of DD models reveal large plumes of burning material (e.g. Khokhlov 1995, 2000; Niemeyer & Hillebrandt 1995). These plumes may leave their imprint on the chemical structure of the ejecta. The plumes do not significantly perturb the density distribution and hence will not explain global asymmetries in the overall density structure (Khokhlov 2000), but could leave an imprint at composition interfaces. WWH97 suggested this mechanism as a possible explanation for the polarization signatures seen in SN 1996X, but these plumes are an unlikely explanation for the global deviations from sphericity with a well-defined axis of symmetry as in SN 1999by.

Livne (1999) pointed out that we cannot expect a deflagration/detonation transition on a sphere as implicitly assumed in spherical models, but that the transition may begin at one point. Detailed 2D calculations showed large scale asymmetries, but Livne only followed the explosion process. He did not follow the calculation into the homologous expansion, which may or may not destroy any initial asphericities by the time of maximum light when the observations of SN 1999by were taken. It is also not clear why such a mechanism should apply to subluminous SNe Ia and not, perhaps, to most SNe Ia.

In any accretion model, we expect an impact of the supernova ejecta with the secondary star. Marietta, Burrows, & Fryxell (2000) computed 2D numerical simulations of the impact of an SN Ia explosion with hydrogen-rich main sequence, subgiant, and red giant companions. They find that the blast strips main sequence and subgiant companions of 15% of their mass while red giants lose $\sim 97\%$ of their envelopes ($0.5 M_{\odot}$). The impact of the ejecta with the secondary star creates a hole in the debris of angular size $\sim 30^{\circ} - 40^{\circ}$, corresponding to $\sim 10\%$ of the ejecta surface. The result was similar for all cases considered because the companion was close enough to be in Roche lobe overflow. This effect may be consistent with the polarization observed in SN 1999by, but we would expect the same effect in both normal and subluminous SNe Ia which may be in conflict with the low polarization observed in normally-bright SNe Ia.

Mahaffey & Hansen (1975) calculated a rotating detonation model, but no detailed models have been calculated for rapidly rotating, deflagrating white dwarfs. Rapid rotation

will produce a global distortion of the density structure of the presupernova WD (Müller & Eriguchi 1985) and may also affect the propagation of nuclear burning fronts in the supernova, resulting in small asphericities. We regard this possibility as very attractive since the combined effect of rotational distortion and modification of the nuclear deflagration front has the potential to link the subluminosity of SN 1999by to the large, global asymmetry. A comparison with Model 7 of Müller & Eriguchi suggests that even with solid body rotation (which produces the minimum distortion for a given angular momentum), sufficient rotation to distort the structure in the silicon layers of our subluminescent model would need to have a rotation energy only about 5% of the gravitational energy. Thus a significant, but not extreme, rotation may be sufficient to explain the degree of polarization we observe in SN 1999by. Rotation could thus serve as a single parameter that distinguishes normal SNe Ia arising in slowly-rotating white dwarf progenitors from subluminescent SNe Ia that occur in more rapidly-rotating white dwarfs. One possible problem with the scenario of rotation as a single parameter is that SN properties appear to show a correlation with environment and by implication, progenitor age (Howell 2000a,b).

In the merging scenario, two C/O white dwarfs merge to produce an SN Ia (Webbink 1984; Iben & Tutukov 1984). This would provide a natural explanation for the lack of hydrogen seen in Ia spectra. There is evidence that such systems exist (Saffer et al. 1998). Khokhlov et al. (1993) and HK96 parameterized merger events as spherically symmetric C/O WDs with thick envelopes. They produced light curves that were in reasonable agreement with some SNe Ia. Doubts about the merger models have been raised. Three-dimensional hydrodynamical simulations of the process show that (unless the system ignites during the merger process) the less massive star is disrupted into a hot envelope and an accretion disk around the primary (Benz et al. 1990; Rasio & Shapiro 1995; Mochkovitch, Guerrero, & Segretain 1997). In this case, off center carbon ignition produces a flame that propagates inward, converting the star to an O+Ne+Mg WD (Nomoto & Iben 1985; Saio & Nomoto 1985, Kawai, Saio, & Nomoto 1987; Saio & Nomoto 1998). Magnesium-24 then undergoes electron capture, inducing accretion-induced collapse, to produce a neutron star (Saio & Nomoto 1985, Mochkovitch & Livio 1990, Nomoto & Kondo 1991). Alternatively, it may be possible to ignite the system due to tidal heating during the merger process (Iben, Tutukov, & Fedorova 1998) which could produce a highly aspherical explosion. This scenario has not been demonstrated in realistic simulations, but deserves further study.

We have to stress the limits of this study which must be seen only as a first step. Clearly, more high quality data must be obtained to provide a statistical sample and to make use of small scale features to evaluate details of the geometry and, ultimately, to probe details of the explosion mechanism (e.g. the burning properties) and the scenario (e.g. rotation of a single rapidly rotating WD vs. merging of two WDs). Future data should have a

noise level well below 0.1% to address questions of deviations from axial symmetry and to utilize the small scale variations seen in the models. This is a very feasible goal with the current and upcoming generation of 8 m class telescopes. Our models are based on aspherical envelopes which are distorted artificially. Although this is a reasonable approach to estimate the size of asphericity and general properties, it hardly provides the desired link to the physical mechanisms responsible. Detailed hydro calculations for the various mechanism are needed. Within the delayed detonation scenario, consistent hydro calculations of rotating WDs, deflagration fronts and the multi-dimensionality of the deflagration to detonation transition are feasible. Although any successful model must reproduce the overall pattern in the chemical composition, alternative scenarios with full multi-dimensional hydrodynamics may do this job as well. In particular, the merging scenario needs more attention.

This research was supported in part by NSF Grant 95-28110, by NASA Grant LSTA-98-022 and a grant from the Texas Advanced Research Program. The calculations were done on a cluster of workstations financed by the John W. Cox Fund of the Department of Astronomy at the University of Texas, and processors donated by Advanced Micro Devices (AMD). We are grateful to A. Filippenko, D. Leonard, and an anonymous referee for discussions and to G. Hill for providing the IGP which made this work possible.

APPENDIX: Computational Methods

1. Radiation-Hydrodynamics and Light Curves in Spherical Geometry

Explosion models are calculated using a one-dimensional radiation-hydro code (HK96) that solves the hydrodynamical equations explicitly by the piecewise parabolic method (Colella & Woodward 1984). Nuclear burning is taken into account using an extended network of 216 isotopes (Thielemann, Nomoto & Hashimoto 1996 and references therein). The propagation of the nuclear burning front is given by the velocity of sound behind the burning front in the case of a detonation wave and in a parameterized form during the deflagration phase based on detailed 3-D calculations (e.g. Khokhlov 1995, 2000; Niemeyer & Hillebrandt 1995). We use the parameterization as described in Dominguez & Höflich (2000). We assume that $v_{\text{burn}} = \max(v_t, v_l)$, where v_l and v_t are the laminar and turbulent velocities with

$$v_t = C_1 \sqrt{\alpha_T g L_f}, \quad [A1]$$

with $C_1 = 0.15$ and with

$$\alpha_T = (\alpha - 1)/(\alpha + 1), \quad [A2]$$

and with

$$\alpha = \rho^+(r_{\text{burn}})/\rho^-(r_{\text{burn}}). \quad [A3]$$

Here α_T is the Atwood number, L_f is the characteristic length scale, and ρ^+ and ρ^- are the densities in front of and behind the burning front, respectively. The quantities α and L_f are directly taken from the hydro at the location of the burning front and for this choice of C_1 we take $L_f = r_{\text{burn}(t)}$. The transition density is treated as a free parameter. The description of the deflagration front does not significantly influence the final structure of the explosion. The amount of matter consumed during burning (and the total ^{56}Ni production) is governed by the pre-expansion of the WD and, consequently, is determined by the transition density ρ_{tr} , at which the burning front switches from the deflagration to the detonation mode (Höfllich 1995a). The value ρ_{tr} can be adjusted to produce a given amount of ^{56}Ni which determines the brightness (Höfllich 1995a) and through the temperature dependence of the opacity, the decline rate (HKW95; Höfllich et al. 1996).

The code also simultaneously solves for the energy and radiation transport with variable Eddington factors. The radiation transfer portion of the code consists of (i) an LTE radiation transfer scheme based on the time-dependent moment equations which are solved implicitly, (ii) a frequency-dependent radiation transport to determine the Eddington factors and the frequency averaged opacities, (iii) a detailed equation of state with an elaborate treatment of the ionization balance and the ionization energies, (iv) time-dependent expansion opacities which take into account the composition structure of the explosion model, (v) photon scattering and thermalization calibrated by NLTE-calculations, and (vi) a Monte Carlo γ -ray deposition scheme which takes into account all relevant γ -ray transitions and interaction processes. For more details, see Höfllich et al. (1999), and references therein.

2. Density and Chemical Structure of the 3-D envelope

Aspherical density structures are constructed from the spherical density distribution by imposing a homologous expansion function which depends on the angle Θ from the equatorial plane and which conserves the total energy and the mass fraction per steradian from the spherical model (Höfllich et al. 1999). The spherical density structure is given by

$$\rho(R, \Theta) = \rho(R), \quad [A4]$$

with R the initial distance of a mass element from the center. Homologous expansion of this density distribution is assumed with a scaling that depends on angle, i.e.,

$$\frac{v(R, \Theta)}{R} = C(\Theta), \quad [A5]$$

so that

$$r(\Theta) = C(\Theta) R t, \quad [A6]$$

where t is the time since the explosion and $r(\Theta)$ is the distance of the mass element after time t .

Because little is known about the general geometry of the ejecta, we construct ellipsoidal isodensity contours with an axis ratio $E = a/b$ at the photosphere where a is the distance of the photosphere in the $x - y$ (symmetry) plane and b is the distance in the (axial) z -direction. This contour is given by

$$r(\Theta) = r(\Theta = 0) \sqrt{(\cos^2(\Theta) + E^2 \sin^2(\Theta))}. \quad [A7]$$

The homology scaling constant, $C(\Theta)$, is determined to produce the desired axis ratio for an ellipsoid (Höflich et al. 1999), and the total explosion energy is normalized to that of the spherical model. Here, the asphericities are small and the temperature profiles in SNe Ia are shallow (HMK93, Höflich 1995a). Therefore, we assume identical isodensity and isotherm contours.

3. Spectra for Asymmetric Configurations

Our radiation transport code works both for spherical geometry and in three dimensions using different modules for the radiation transport. For details and references to the atomic database, see Höflich (1995a) and references therein. The density and abundance structure is taken from the hydro calculations. Excitation due to γ -rays is included via the Monte Carlo code. Based on the list of atomic data of Kurucz (1995), we have constructed detailed atomic models for a couple of ions similar to those used in WWH97. The use of 3-D geometries caused some restrictions on the complexity of the atomic models. Multi-level atoms have been restricted to the main ionization species of C I (23/57), O I (28/75), Mg II (25/85), Si II (28/83), Ca II (26/90) of the intermediate mass elements. Here, the numbers in the parentheses denote the number of levels and of line transitions, respectively. For those ions, the statistical equations are solved consistently including bound-bound and bound-free transitions. The method of accelerated lambda iteration is applied to remove the global dependence of the level populations and the radiation field. In order to include the line blocking effect, about 1,000,000 additional lines are taken into account under the assumption of local thermodynamical equilibrium for the population number but including scattering terms calibrated by the NLTE-elements. The electron temperature structure is based on the depth-dependent luminosity from the monochromatic light curve calculation at a certain time. The complete system of equations is given by the time-independent radiation transport and the statistical equations, i.e., the rate equation, the particle conservation equation, and the charge conservation equation. All allowed bound-bound and bound-free transitions between the NLTE levels are taken into account. Complete redistribution over each individual line both in frequency and in angle are assumed (Mihalas 1978) in the co-moving frame (but not the observer's frame). This means that the populations of sublevels of the upper and lower transition are described by a Maxwell-Boltzman distribution and that the light becomes unpolarized.

3.1 Radiation Transport in 3-D NLTE-Spectra

The current calculations use a modified version of the Monte-Carlo code previously applied to calculate the continuum in SN 1987A (H91) and line polarization in SN 1993J and SN 1996X (Höflich et al. 1995b; WWH97). The code is capable of handling arbitrary 3-dimensional geometries, both for the density and the distribution of the sources. Polarization and flux spectra for rapidly expanding envelopes can thus be computed. Polarization is treated within the Stokes formalism (see, e.g., Van de Hulst, 1957). We include electron scattering as a polarization process but omit scattering at dust particles.

The modifications for the present work to the previous versions of our Monte Carlo scheme (H91) are mainly related to the inclusion of NLTE-effects. In scattering dominated atmospheres, deviations from local thermodynamic equilibrium are also relevant at large optical depths; however, at large optical depths, Monte-Carlo methods become very costly and/or inaccurate (Höflich et al. 1995b). Therefore, we use a hybrid scheme of Monte-Carlo and non-equilibrium diffusion methods. In the latter case, we implicitly solve the time dependent radiation transport equation in a non-equilibrium, diffusion approximation for 3-D geometry including the scattering and thermalization terms for the source functions and include the frequency derivatives in the formulation for the opacities and emissivities (Lucy & Solomon 1970; Karp et al. 1977). At large optical depths, this provides the solution for the full radiation transport problem. We note that the use of a non-equilibrium diffusion does *not* imply that the mean intensity J is given by the black body field. To obtain the correction solution for the radiation transport equation at small optical depths, the difference between the solution of the diffusion and full radiation transport equation is calculated by a Monte Carlo method. We calculate the difference between the solutions for computational accuracy and efficiency. Consistency between the solution at the outer and inner region is obtained iteratively. The same Monte Carlo solver is used which has been applied to compute γ -ray and polarization spectra (e.g. Höflich et al. 1995b). The Monte Carlo method is appropriate for this problem because of its flexibility with respect to the geometrical and velocity structures.

3.2 Coupling of the Radiation Transport and Rate Equations

The solution of the radiation transport and the statistical equations for the level populations are coupled. A perturbation method is used to obtain consistency between the solutions (Höflich 1995a). In the equations for the microphysical quantities we express the actual mean intensity J_ν by the following equation:

$$J_\nu^{(m)} = \Lambda_\nu^{(m)} S_\nu^{(m)} \approx \Lambda_\nu^{(m-1)} S_\nu^{(m-1)} + \Lambda_\nu^{*(m-1)} (S_\nu^{(m)} - S_\nu^{(m-1)}). \quad [A8]$$

Here, the indices in brackets denote the iteration step, and S_ν and Λ_ν are the source function and the radiation transport matrices, respectively. The matrix Λ^* is a band-matrix with elements corresponding to the diagonal and first off-diagonal elements of the complete matrix Λ . The elements of Λ are computed in the narrow line limit (Sobolev et al. 1957; Höflich 1995a).

The use of a Monte-Carlo scheme introduces an additional complication due to the “photon” noise. To achieve numerical stability for the solution in the rate equations, the deviation from the solution for J_ν obtained by the Monte-Carlo calculations and the non-equilibrium diffusion are set to zero if they are less than the statistical noise. This avoids instabilities during the model iterations when using the accelerated lambda iteration technique; however, this also implies an increase of the computational expense with increasing rate of convergence. To increase the photon statistics, solutions of the Monte-Carlo calculation from previous iterations, n , are taken into account with individual weight factors. Currently, we use a $1/(m - n + 1)$ weight where m is the total number of model iterations. Clearly, this weight function needs further fine tuning. Tests for realistic structures of the envelope show that the resulting error in the population numbers inherent to our procedure is comparable to those introduced by discretization errors if we solve the radiation transport equation in a difference scheme.

REFERENCES

- Arbour, R., Papenkova, M., Li, W. D., Filippenko, A. V., & Armstrong, M. 1999, IAUC 7156
- Benz W., Cameron, A. G. W., Press, W. H., & Bowers, R. L. 1990, ApJ, 348, 647
- Bonanos, A., Garnavich, P., Schlegel, E., Jha, S., Challis, P., Kirshner, R., Hatano, K., & Branch, D. 1999, AAS, 195, 3806
- Branch D., & Tammann G.A, 1992, ARAA, 30, 359
- Burstein, D., & Heiles, C. 1982, AJ, 87, 1165
- Chandrasekhar, S. 1960, Radiative Transfer, (New York: Dover)
- Collela, P., & Woodward, P.R. 1984, J.Comp.Phys., 54, 174
- Cropper, M., et al. 1988, MNRAS, 231, 695
- Dominguez I., & Höflich P. 2000, ApJ, 528, 854
- Filippenko, A. V., et al. 1992, AJ, 104, 1543 (F92)
- Gerardy, C.L, Höflich P., Fesen R., & Wheeler J.C. 2000, ApJ, in preparation
- Goodrich, R. G. 1991, PASP, 103, 1314
- Hamuy, M., et al. 1994, AJ, 108, 2226
- Hamuy, M., et al. 1996a, AJ, 112, 2391
- Hamuy, M., Phillips, M. M., Maza, J., Suntzeff, N. B., Schommer, R. A., & Avilés, R. 1995, AJ, 109, 1
- Hamuy, M., Phillips, M. M., Schommer, R. A., Suntzeff, N. B., Maza, J., & Avilés, R. 1996b, AJ, 112, 2398
- Hernandez, I., et al. 2000, MNRAS, submitted (astro-ph/0007022)
- Höflich, P. 1991, A&A, 246, 481 (H91)
- Höflich, P. 1995a, ApJ, 440, 821
- Höflich, P. 1995b, ApJ, 443, 89

- Höflich, P., Dominik, C., Khokhlov, A., Müller, E., & Wheeler, J.C. 1996, *17th Texas Symposium on Relativistic Astrophysics*, Annals of the New York Academy of Science, 759, 348
- Höflich, P., & Khokhlov, A. 1996, ApJ, 457, 500 (HK96)
- Höflich, P., Khokhlov, A., & Wheeler, J. C. 1995a, ApJ, 444, 831 (HKW95)
- Höflich, P., Khokhlov A., Wheeler, J. C., Phillips, M. M., Suntzeff, N. B., & Hamuy, M. 1996, ApJ, 472, L81
- Höflich, P., Müller, E., & Khokhlov, A. M. 1993, A&A, 268, 570 (HMK93)
- Höflich, P., Nomoto, K., Umeda, H., & Wheeler, J.C. 2000, ApJ, 528, 854
- Höflich, P., Wang, L., Wheeler, J. C. 1999, ApJ, 521, 179
- Höflich, P., Wheeler, J. C., Hines, D., & Trammell, S. 1995b, ApJ, 459, 307
- Howell, D. A. 2000a, PhD Thesis, University of Texas
- Howell, D. A. 2000b, in preparation
- Hough, J. H., Bailey, J. A., Rouse, M. F., & Whittet, D. C. B. 1987, MNRAS, 227, 1P
- Hoyle, F., & Fowler, W. A. 1960, ApJ, 132, 565
- Iben, I., & Tutukov, A. V. 1984, ApJS, 54, 335
- Iben, I., Tutukov, A. V., & Fedorova, A. 1998, ApJ, 503, 344
- Iwamoto, K., Brachwitz, F., Nomoto, K., Kishimoto, N., Umeda, H., Hix, W. R., & Thielemann, F. K. 1999, ApJS 125, 439
- Jeffery, D. 1991, ApJ, 375, 264 (J91)
- Karp, A. H., Lasher, G., Chan, K. L., & Salpeter, E. E. 1977, ApJ, 214, 161
- Khokhlov, A. 1991, A&A, 245, 114
- Khokhlov, A., Müller, E., & Höflich, P. 1993, A&A, 270, 223
- Khokhlov, A. 1995, ApJ, 449, 695
- Khokhlov, A. 2000, ApJ, submitted (astro-ph/0008463)

- Kurucz, R.L. 1995, CD-23, Center for Astrophysics
- Kawai, Y., Saio, H., & Nomoto, K. 1987, ApJ, 315, 229
- Leibundgut, B., et al. 1993, AJ, 105, 301
- Lentz, E. J., Baron, E., Branch, D., Hauschildt, P., & Nugent, P. 1999, ApJ, 527, 746
- Leonard, D.C., Filippenko, A. V., & Matheson, T. 2000a in *Cosmic Explosions*, eds. S. S. Holt & W. W. Zhang, (Melville, NY: AIP), p. 165
- Leonard, D.C., Filippenko, A. V., Ardila, D. R., & Brotherton, M. S. 2000b, ApJ, submitted, astro-ph/0009285
- Li, W.-D., Filippenko, A. V., Treffers, R. R., Riess, A. G., Hu, J., & Qiu, Y. 2000, ApJ, submitted (astro-ph/0006292)
- Li, W.-D., Modjaz, M., King, J. Y., Papenkova, M., Johnson, R. A., Friedman, A., Treffers, R. R., & Filippenko, A. V. 1999, IAUC 7126
- Livne, E. 1999, ApJ, 527, L97
- Lucy, L.B., & Solomon, P.M. 1970, ApJ 159, 879
- Mahaffy, J. H., & Hansen, C. J. 1975, ApJ, 201, 695
- Marietta, E., Burrows, A., & Fryxell, B. 2000, ApJS, 128, 615
- Mathewson, D. S., & Ford, V. 1970, Mem. RAS, 74, 139
- Mathewson, D. S., Ford, V., Klare G., Neckel, T., & Krautter, J. 1978, Bull. Inform. CDS, 14, 115
- Mazzali, P. A., et al. 1997, MNRAS, 284, 151
- McCall, M. L., Reid, N., Bessell, M. S., & Wickramasinghe, D. 1984a, MNRAS, 210, 839
- McCall, M. L., Reid, N., Bessell, M. S., & Wickramasinghe, D. 1984b, MNRAS, 211, 991
- Mihalas, D. 1978, *Stellar Atmospheres*, (San Francisco: Freeman)
- Miller, J. S., Robinson, L. B., & Goodrich, R. W. 1988, in *Instrumentation for Ground-Based Optical Astronomy, Present and Future*, ed. L.B. Robinson, (New York: Springer-Verlag)

- Milne P., The, L.S., & Leising, M.D. 1999, ApJS 124, 503
- Mochkovitch, R. Guerrero, J., & Segretain, L. 1997, in *Thermonuclear Supernovae*, eds. Ruiz-Lapuente, Canal, & Isern 1997, (Dordrecht: Kluwer), pp. 187
- Mochkovitch, R., & Livio, M. 1990, A&A, 236, 378
- Modjaz, M., et al. 2000, PASP, submitted (astro-ph/0008012)
- Müller, E., & Eriguchi, Y. 1985, A&A, 152, 325
- Niemeyer, J. C., & Hillebrandt, W. 1995, ApJ, 452, 779
- Nomoto, K. 1980, ApJ, 248, 798
- Nomoto, K., & Iben, I. J. 1985, ApJ, 297, 531
- Nomoto, K., & Kondo Y. 1991, ApJ, 367, L19
- Nomoto, K., & Sugimoto, D. 1977, PASJ, 29, 765
- Nomoto, K., Thielemann, F. K., & Yokoi, K. 1984, ApJ, 286, 644
- Nugent, P., Baron, E., Hauschildt, P., & Branch., D. 1997, ApJ, 485, 812
- Nugent, P., Phillips, M. M., Baron, E., Branch, D., & Hauschildt, P. 1995, ApJ, 455L, 147 (N95)
- Paczynski B. 1985, in *Cataclysmic Variables and Low-Mass X-Ray Binaries*, eds. D.Q. Lamb & J. Patterson, (Dordrecht: Reidel) p. 1
- Perlmutter, S., et al. 1997, ApJ, 483, 565
- Perlmutter, S., et al. 1999, ApJ, 517, 565
- Phillips, M. 1993, ApJ, 413, L105
- Rasio, F. A., & Shapiro, S. L. 1995, ApJ, 438, 887
- Riess, A. G., et al. 1999, AJ, 117, 707
- Riess, A. G., Press, W. H., & Kirshner, R. P. 1996, ApJ, 473, 88
- Ruiz-Lapuente, P., Jeffery, D. J., Challis, P., Filippenko, A. V., Kirshner, R. P., Ho, L. C., Schmidt, B. P., Sanchez, F., & Canal, R. 1993, Nature 365, 728

- Saffer, R. A., Livio, M., & Yungelson, L. R., 1998, *ApJ*, 502, 394
- Saio, H., & Nomoto, K. 1985, *A&A*, 150, L21
- Saio, H., & Nomoto, K. 1998, *ApJ*, 500, 388
- Savage, B. D., & Mathis, J. S. 1979, *ARAA*, 17, 73
- Schaefer, B. E. 1996, *ApJ*, 464, 404
- Schlegel, D. J., Finkbeiner, D. P., & Davis, M. 1998, *ApJ*, 500, 525
- Schmidt, B. P., et al. 1998, *ApJ* 507, 46
- Serkowski, K., Mathewson, D., & Ford, V. L. 1975, *ApJ*, 196, 261
- Shakhovskoi, N. M. 1976, *Soviet Astron. Lett.*, 2, 107
- Shapiro, P. R., & Sutherland, P. G. 1982, *ApJ*, 263, 902
- Simmons, J. F. L., & Stewart, B. G. 1985, *A&A*, 142, 100
- Sobolev, V. V. 1957, *Sov. Astron.* 1, 297
- Spyromilio, J., & Bailey, J. 1993, *PASAu*, 10, 263S
- Thielemann F.-K., Nomoto K., & Hashimoto M. 1996, *ApJ*, 460, 408
- Trammell, S. R. 1994, PhD Thesis, University of Texas, pp. 246-260
- Tran, H. D. 1995, *ApJ*, 440, 578
- Treffers, R. R., Peng, C. Y., Filippenko, A. V., & Richmond, M. W., 1997, *IAUC* 6627
- Turatto, M., et al. 1996, *MNRAS*, 283, 1
- Turatto, M., Piemonte, A., Benetti, S., Cappellaro, E., Mazzali, P. A., Danziger, I. J., & Patat, F. 1998, *AJ*, 116, 2341
- Umeda, H., Nomoto, K., Yamaoka, H., & Wanajo S. 1999, *ApJ*, 513, 861
- Van de Hulst, H.C. 1957, *Light Scattering by Small Particles*, (New York: Wiley)
- Wang, L., Baade, D., Fransson, C., Höflich, P., & Wheeler, J. C. 2000b, *ApJ*, submitted
- Wang, L., Howell, D. A., Höflich, P., & Wheeler, J. C. 2000a, *ApJ*, submitted (astro-ph/9912033)

- Wang, L., & Wheeler, J. C. 1996, *ApJ*, 462, L27
- Wang, L., Wheeler, J. C., & Höflich, P. 1997a, *ApJ*, 476, L27 (WWH97)
- Wang, L., Wheeler, J. C., & Höflich, P. 1997b, in *SN1987A, Ten Years After*, eds. M. M. Phillips & N. Suntzeff, (New York: Kluwer), in press
- Wang, L., Wheeler, J. C., Li, Z., & Clocchiatti, A. 1996, *ApJ*, 467, 435
- Webb, W., Malkan, M., Schmidt, G., & Impey, C. 1993, *ApJ*, 419, 494
- Webbink, R. F. 1984, *ApJ*, 277, 355
- Wheeler, J. C., Höflich, P., Harkness, R. P., & Spyromilio, J. 1998, *ApJ*, 496, 908
- White, R. L. 1979, *ApJ*, 229, 954
- Whittet, D. C. B., Martin, P. G., Hough, J. H., Rouse, M. F., Bailey, J. A., & Axon, D. J. 1992, *ApJ*, 386, 562
- Wolstencroft, R. D., & Kemp, J. C. 1972, *Nature*, 238, 452
- Woosley, S. E., & Weaver, T. A. 1994, *ApJ*, 423, 371
- Woosley S.E., & Weaver T.A. 1986, *ARAA*, 24, 205
- Yamaoka H., Nomoto K., Shigeyama T., & Thielemann F., 1992, *ApJ*, 393, 55

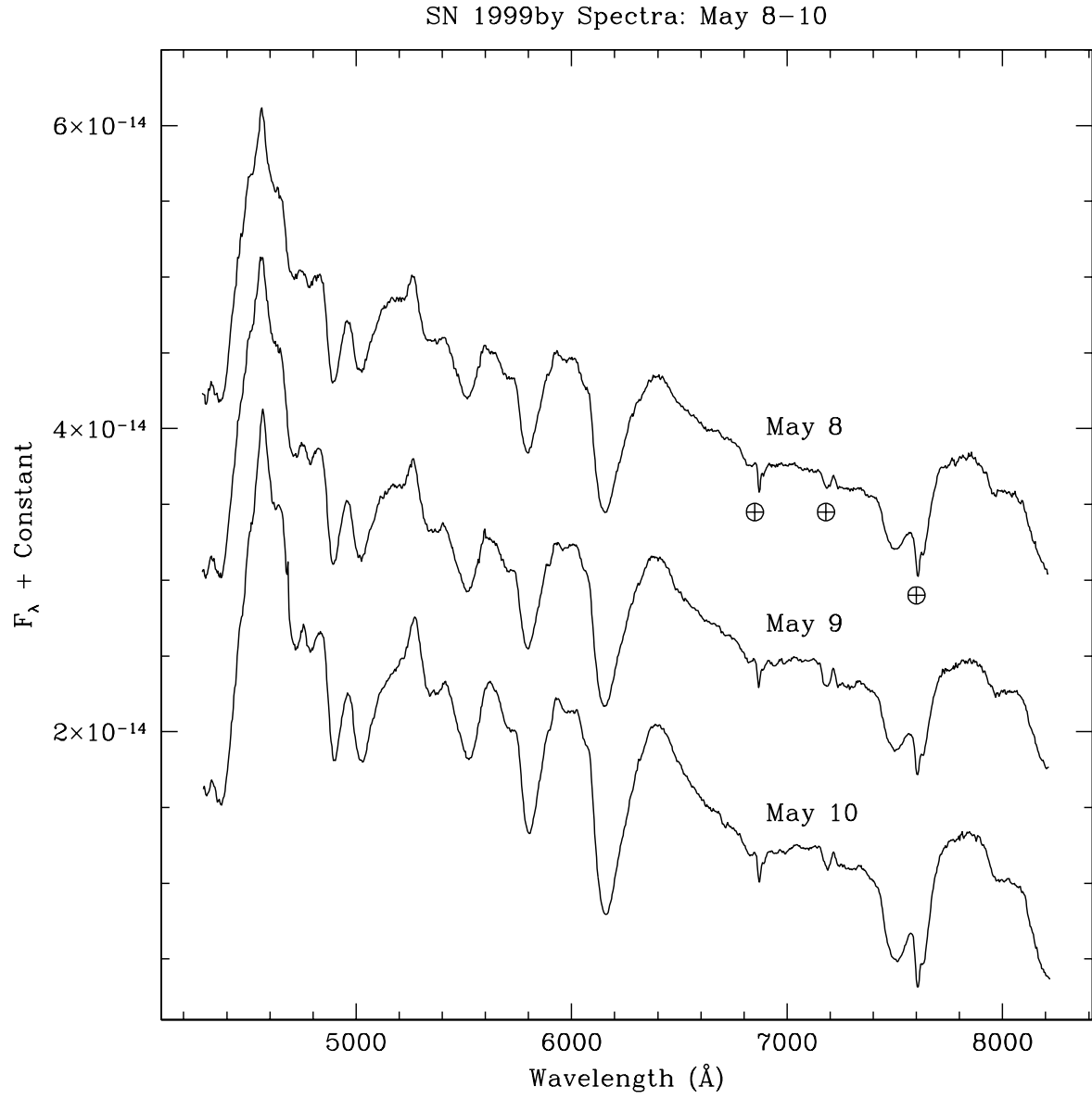


Fig. 1.— Flux spectra of SN 1999by at -2 days, -1 day, and *B* maximum. The data are in arbitrary units. Earth symbols denote terrestrial atmospheric features.

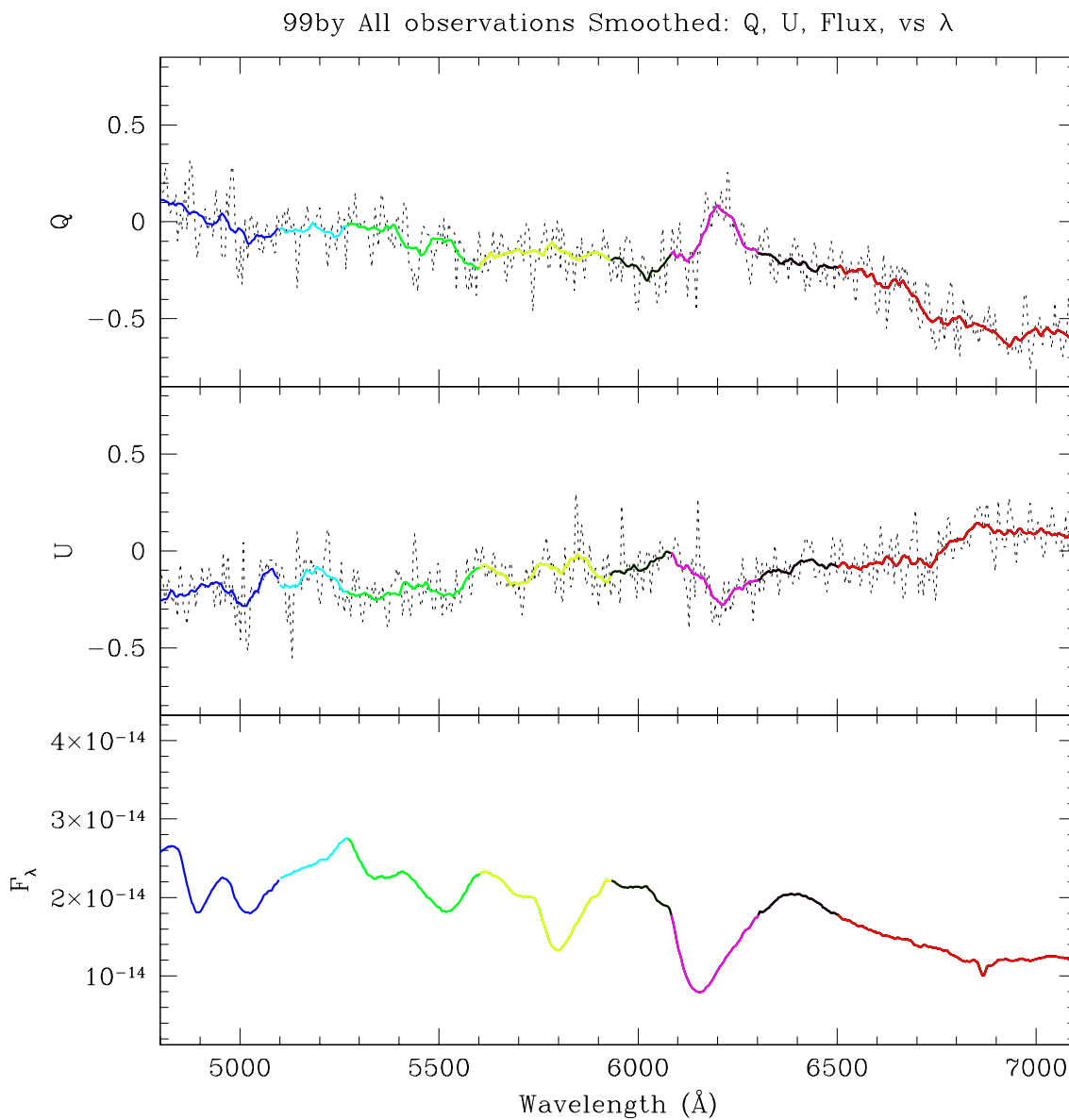


Fig. 2.— Unsmoothed (dashed line) and smoothed, color coded Q , U , and flux spectra of SN 1999by created by summing all observations. Features from 4800–5100 Å are blue, from 5100–5270 Å light blue. The S II features from 5270 to 5600 are green. The Si II 5800 Å feature is yellow, while the Si II 6150 Å line is magenta. Black represents the area between the Si features and the area slightly redward. The large, broad polarization feature to the red of 6500 Å is colored red. Colors are the same as in Figure 4.

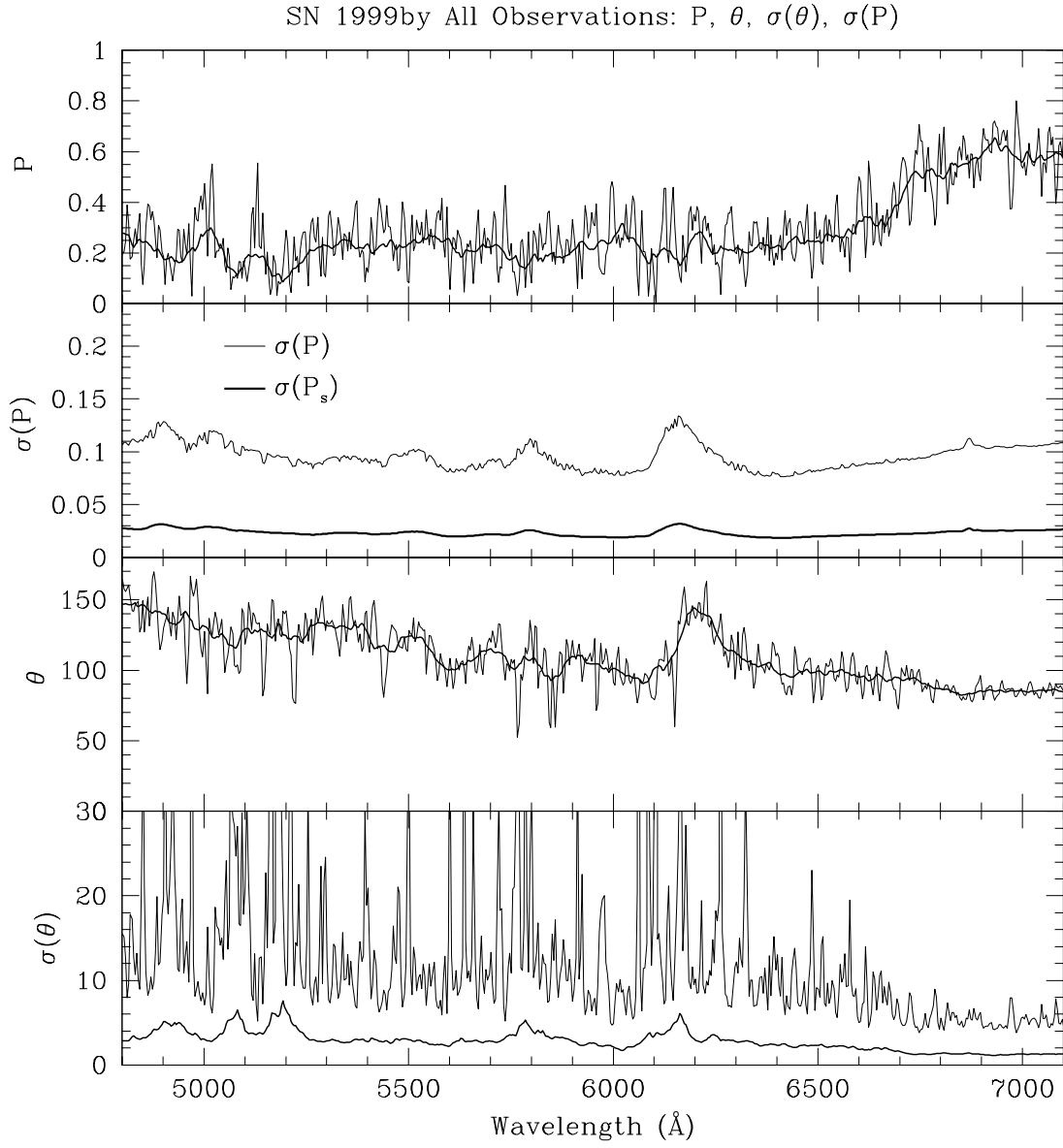


Fig. 3.— P , Θ , $\sigma(\Theta)$, $\sigma(P)$ for SN 1999by created by summing all observations.

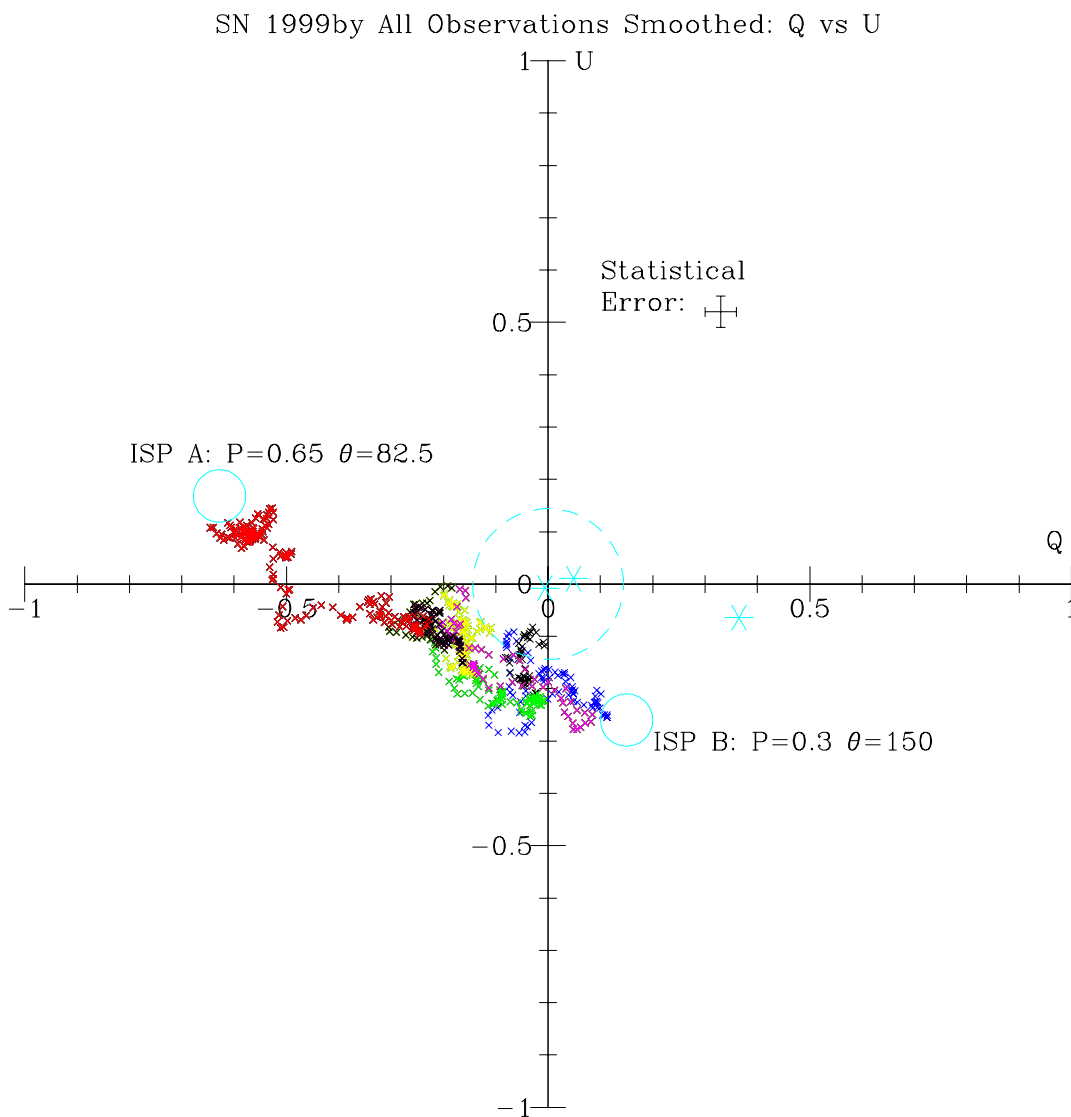


Fig. 4.— Smoothed, color coded $Q - U$ plane for SN 1999by created by summing all observations. Each point corresponds to one pixel in the spectrum. Error bars are statistical error bars for the smoothed data. Light blue asterisks are polarization measurements of stars in the Galaxy within 5° of the line of sight of the SN. Light blue circles denote two choices of ISP discussed in the text. The diameter of these circles corresponds to the approximate uncertainty in the placement of the ISP using the empirical method. Dashed circle is the maximum allowable interstellar polarization from the Galaxy, as discussed in the text. Colors are the same as in Figure 2.

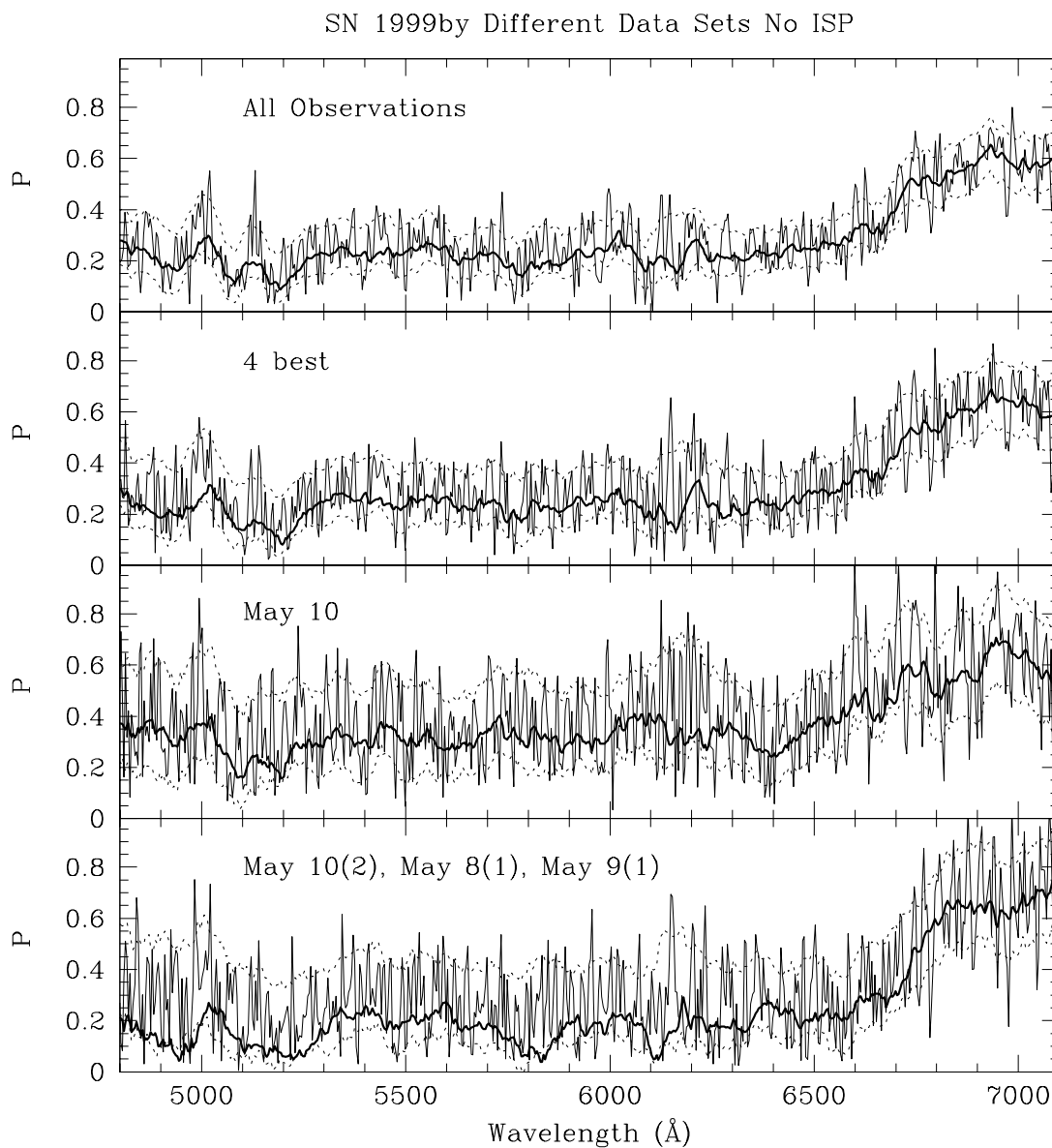


Fig. 5.— Different data sets of P for SN 1999by. Top panel: all observations combined. Second panel: The 4 best sets of observations. Third panel: The best single data set — the first data set taken on the night of maximum light, May 10. Last panel: similar to the “4 best” case, but without the best spectrum (May 10-1). This is the sum of the data sets May 8-1, May 9-1, and May 10-2 — the 2nd through 4th best sets.

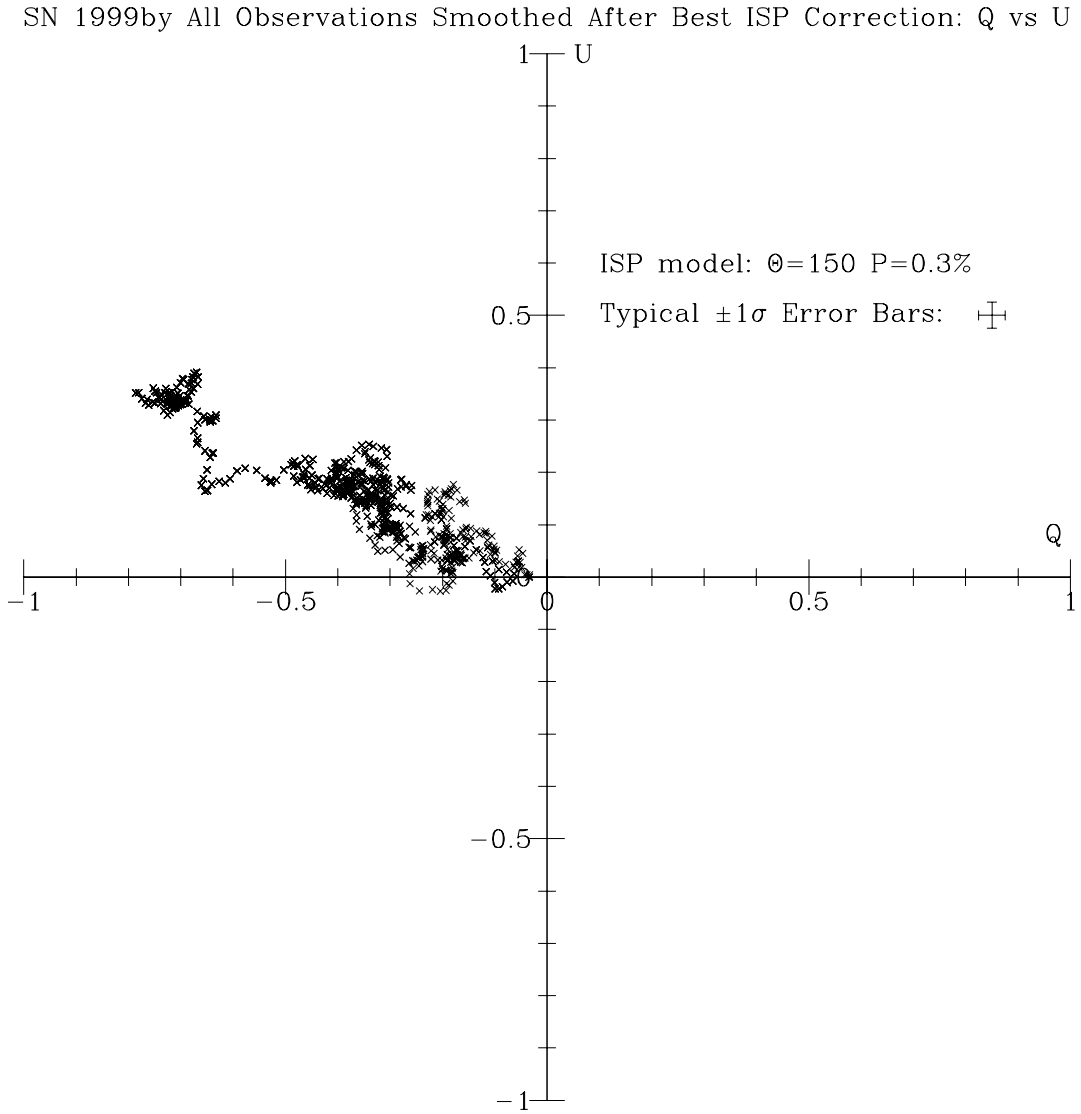


Fig. 6.— All observations: Q , U , P and θ for SN 1999by after subtraction of P_{ISP} . A. The resulting polarization spectrum argues against this choice on theoretical grounds.

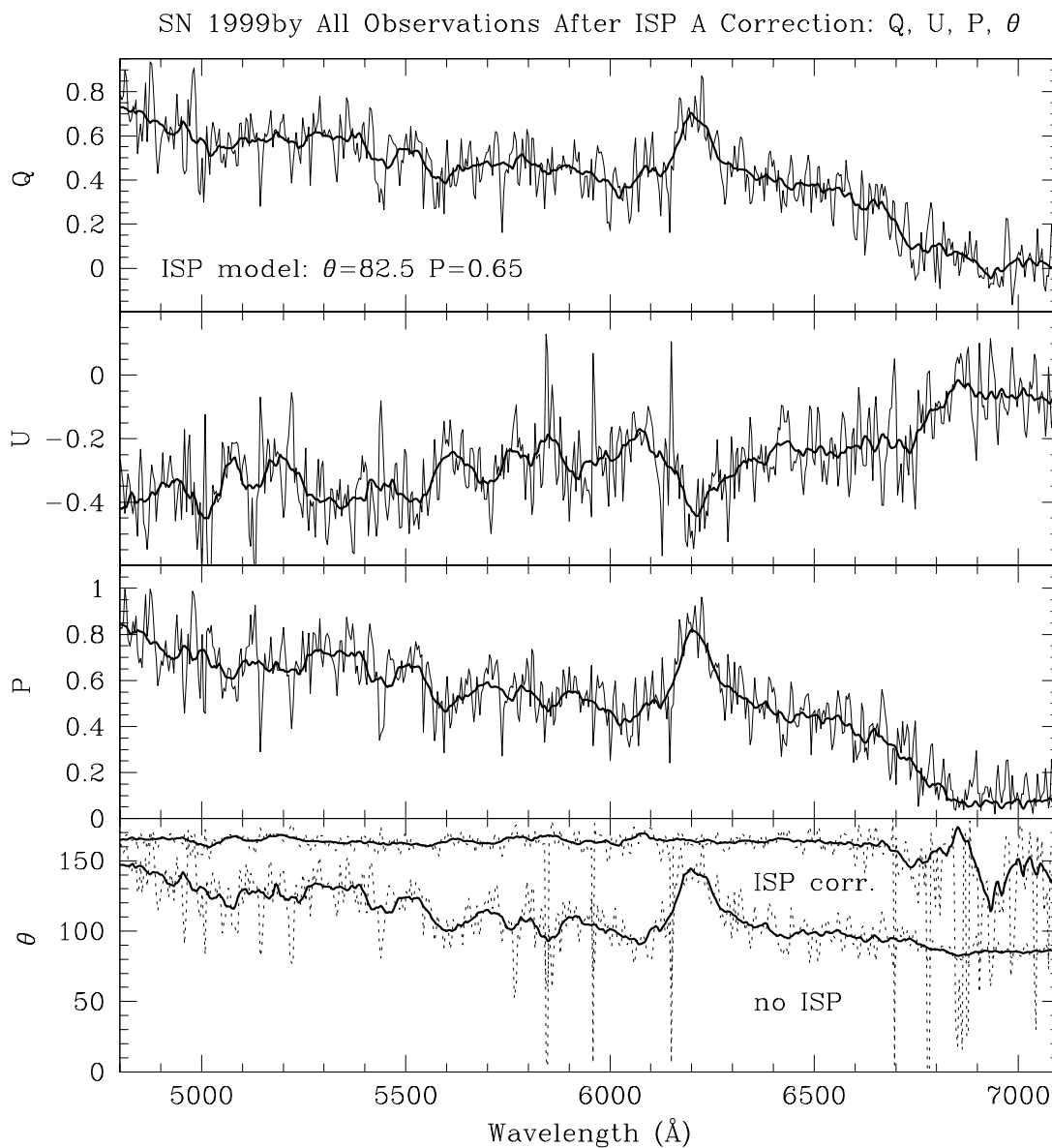


Fig. 7.— The data in the $Q - U$ plane as in Figure 4 after correction for P_{ISPB} with $P_{ISP} = 0.3\%$, $\Theta_{ISP} = 150^\circ$. This ISP has been vector subtracted from each point in accordance with the Serkowski law. The resulting distribution of points for SN 1999by is consistent with a constant polarization position angle, $\Theta = 80^\circ$ across all wavelengths.

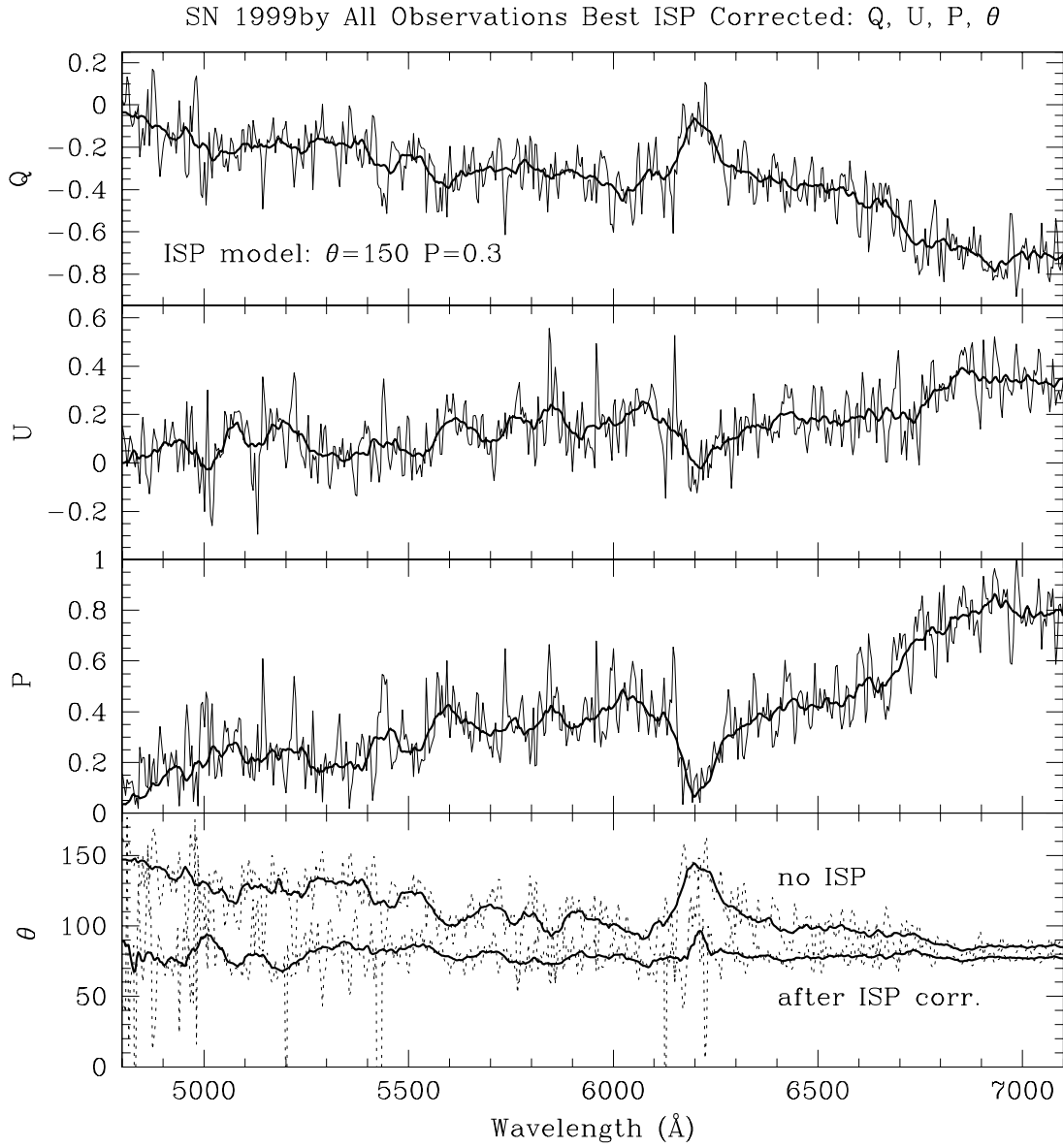


Fig. 8.— All observations: Q , U , P and Θ for SN 1999by corrected for ISP B. Note that after ISP correction, Θ is nearly constant with wavelength.

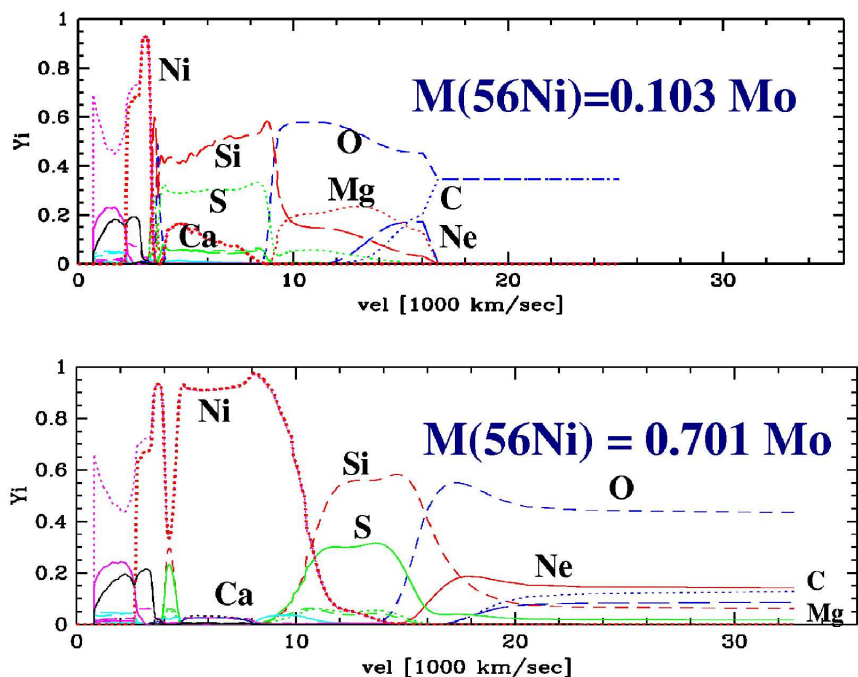


Fig. 9.— Final chemical structures of models are given for a strongly subluminous (top panel) and a normally-bright (bottom panel) supernova during the phase of homologous expansion. Identical progenitors and prescription for the deflagration and detonation fronts have been used but the deflagration-detonation transition density, ρ_{tr} , of $1 \times 10^7 \text{ g cm}^{-3}$ and $2.5 \times 10^7 \text{ g cm}^{-3}$ have been used to produce the subluminous and normally-bright models, respectively. Note that in the subluminous model, ^{56}Ni is confined to a lower region of velocity space, beneath the optical photosphere at maximum light.

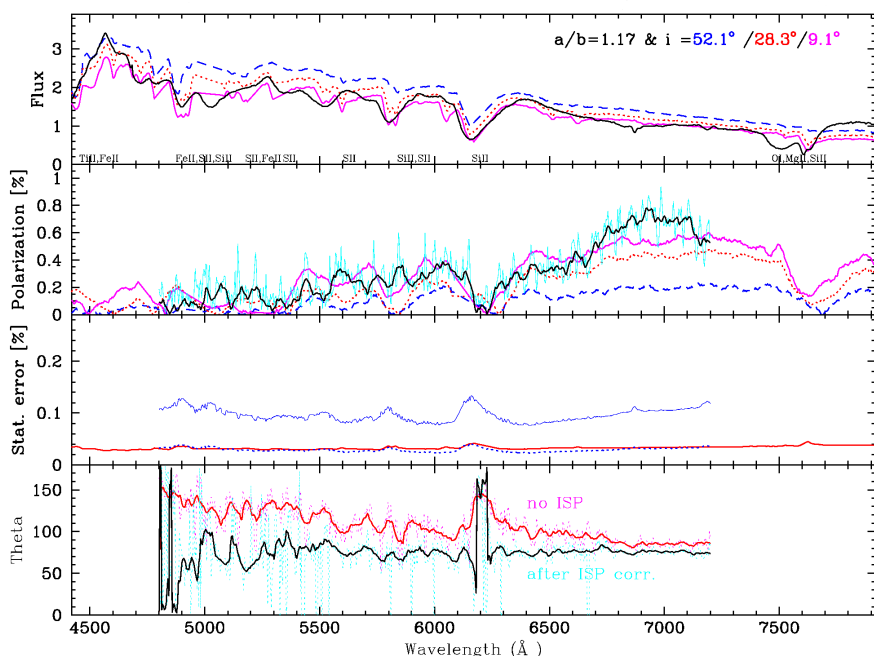


Fig. 10.— Flux spectra (top panel) and polarization spectra (second panel) at day 15 after the explosion for a subluminal delayed-detonation model (see text). The observations are not corrected for reddening, since it is uncertain, though they are corrected for the negligible redshift ($z = 0.00213$). The model SN has been mapped into an oblate ellipsoid with axis ratio 1.17 shown for various inclinations i and compared to the observations of SN 1999by at about maximum light in B (see §2). For comparison with the models, an interstellar component with $P = 0.25\%$ and $\Theta = 140^\circ$ has been subtracted from the observations. The observed flux spectrum is the solid black line. Model flux spectra are shown by solid magenta, dotted red, and dashed blue lines for inclination angles, i , of 9.1° , 28.3° , and 52.1° , respectively. In the second panel, the raw polarization data is shown by a light blue line, while the smoothed data (with $\Delta\lambda = 45\text{\AA}$) is the black line. The model polarization spectra are the same as the first panel. The third panel presents the statistical error in P for the raw data (blue), smoothed data (dotted blue), and theoretical model (red; binned to $\Delta\lambda = 12.5\text{\AA}$). The model seen nearly equator-on ($i = 9.1^\circ$) does the best job of reproducing the general features of the polarization spectrum: depolarization from 4900\AA to 5500\AA , moderate polarization from 5500\AA to 6100\AA , a depolarization in the Si 6150\AA feature, and a rising polarization to the red. In the bottom panel, the observed polarization angle Θ is shown as a function of wavelength. The unbinned data are given by dashed lines and the binned data by solid lines. The data are shown before and after correcting for the ISP contribution determined from the models (see text). After correction for ISP is clear that the position angle is essentially constant across all wavelengths. There is an 80° shift across the Si II trough feature, though this is an artifact of low polarization close to the origin giving an uncertain position angle. Compare this choice of ISP to the empirically determined choice, Figure 8.

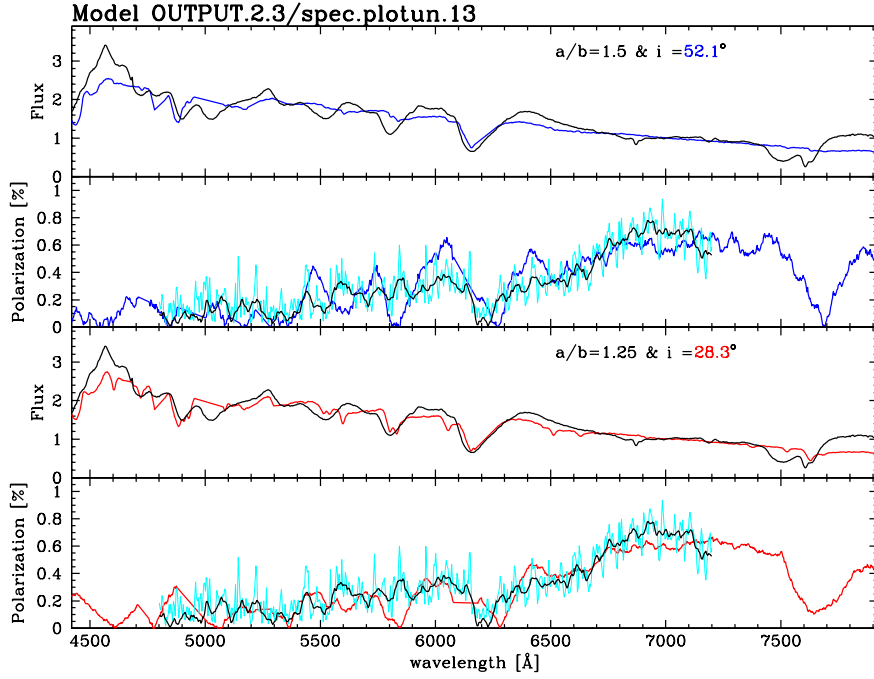


Fig. 11.— Same as Figure 10 but with $a/b = 1.5$ and $i = 52.1^\circ$ (upper two panels) and with $a/b = 1.25$ and $i = 28.3^\circ$ (lower two panels) in comparison with the observations of SN 1999by. These models, particularly the model with $i = 52.1^\circ$ do not match the data as well as the nearly edge-on geometry of Figure 10.

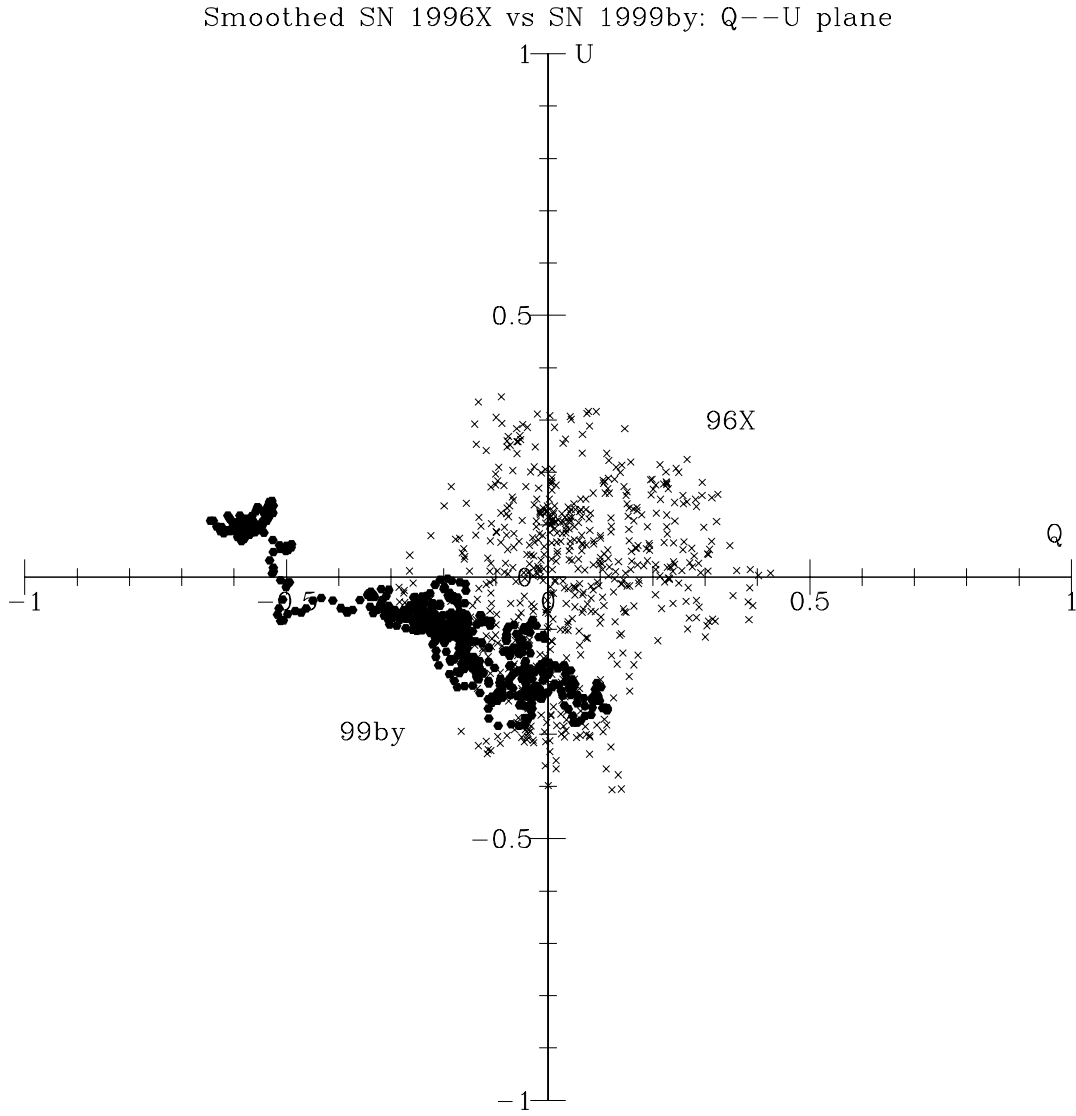


Fig. 12.— Smoothed, $Q - U$ plane for SN 1999by vs SN 1996X created by summing all observations. Red crosses are SN 1996X and blue solid points are SN 1999by.

Table 1. Observing Log

Object	Exptime ^a (s)	UT Start ^b (h:m)	UT Date (m/d/y)	PA ^c (°)	Type ^d	Par ^e (°)	X ^f
SN1999by	1200	4:25	5/8/99	0	o	11.8	1.31
SN1999by	1200	4:47	5/8/99	45	o	6.9	1.38
SN1999by	1200	5:10	5/8/99	22.5	o	2.1	1.47
SN1999by	1200	5:32	5/8/99	67.5	o	-2.2	1.58
SN1999by	1200	6:03	5/8/99	0	o	-7.9	1.77
SN1999by	1200	6:25	5/8/99	45	o	-7.3	1.94
SN1999by	1200	6:47	5/8/99	22.5	o	-15.6	2.16
SN1999by	1200	7:08	5/8/99	67.5	o	-19.2	2.42
HD 154445	3	9:55	5/8/99	0	p	68.1	1.21
HD 154445	3	9:56	5/8/99	45	p	67.8	1.21
HD 154445	3	9:57	5/8/99	22.5	p	67.4	1.21
HD 154445	3	9:58	5/8/99	67.5	p	67.1	1.22
HD 192281	25	10:26	5/8/99	0	f	17.7	1.08
HD 245310	240	3:02	5/9/99	0	p	-27.4	3.70
HD 245310	240	3:07	5/9/99	45	p	-27.7	3.96
HD 245310	240	3:14	5/9/99	22.5	p	-28.1	4.39
HD 245310	240	3:19	5/9/99	67.6	p	-28.4	4.76
SN 1999by	1800	4:22	5/9/99	0	o	11.6	1.31
SN 1999by	1800	4:58	5/9/99	45	o	3.7	1.44
SN 1999by	1800	5:31	5/9/99	22.5	o	-2.7	1.60
SN 1999by	1800	6:04	5/9/99	67.5	o	-8.8	1.81
SN 1999by	1800	6:40	5/9/99	0	o	-15.1	2.13
SN 1999by	1800	6:56	5/9/99	45	o	-17.9	2.31
SN 1999by	1800	7:12	5/9/99	22.5	o	-20.6	2.53
SN 1999by	1800	7:28	5/9/99	67.5	o	-23.3	2.80
HD 155528	120	8:49	5/9/99	0	p	85.3	1.22
HD 155528	120	8:52	5/9/99	22.5	p	86.5	1.22
HD 155528	120	8:55	5/9/99	45	p	87.6	1.22
HD 155528	120	8:59	5/9/99	67.5	p	89.1	1.22
BD +40 4032	240	9:42	5/9/99	0	f	10.3	1.14
SN1999by	1800	3:07	5/10/99	0	o	32.6	1.15
SN1999by	1800	3:39	5/10/99	45	o	22.6	1.20
SN1999by	1800	4:12	5/10/99	22.5	o	13.9	1.28
SN1999by	1800	4:46	5/10/99	67.5	o	6.2	1.39

Table 1—Continued

Object	Exptime ^a (s)	UT Start ^b (h:m)	UT Date (m/d/y)	PA ^c (°)	Type ^d	Par ^e (°)	X ^f
SN1999by	1200	5:21	5/10/99	0	o	-0.8	1.54
SN1999by	1200	5:42	5/10/99	45	o	-4.8	1.66
SN1999by	1200	6:03	5/10/99	22.5	o	-8.6	1.80
SN1999by	1200	6:24	5/10/99	67.5	o	-12.3	1.97
BD +22 3782	180	8:30	5/10/99	0	p	20.5	1.31
BD +22 3782	180	8:35	5/10/99	45	p	20.5	1.29
BD +22 3782	180	8:39	5/10/99	22.5	p	20.5	1.27
BD +22 3782	180	8:43	5/10/99	67.5	p	20.6	1.26
BD +25 3941	240	9:01	5/10/99	0	f	26.6	1.19

^aExposure time

^bUT at Observation Start

^cWaveplate Position Angle

^dObservation type: o=object (SN), p=polariz. std., f=flux std.

^eSlit orientation with respect to Parallaxial Angle

^fAirmass

May 8 Weather Note — Clear. Moonrise 7:26 UT, after SN obs.

May 9 Weather Note — Some clouds scattered at beginning of night, dissipated.

Moonrise 8:08 UT, after SN obs.

May 10 Weather Note — Some clouds scattered at beginning of night, quickly dissipated. Wind picked up towards the end of the night. Moonrise 8:49 UT, after SN obs.

Table 2. SNe Ia with polarization measurements

SN	Galaxy	Spec ^a	Sub ^b	Epoch ^c	p (%)	Detection ^d	Ref.
1972E	NGC 5253	b	n	30:	0.35±0.2	Undetermined	1
1975N	NGC 7723	b	n:	0:, 34:	1.5	ISP	2
1981B	NGC 4536	b	n	56	0.41±0.14	Undetermined	3
1983G	NGC 4753	s	n:	-2:	2.0	Upper limit	4
1986G	NGC 5128	b	s	-9,-8	5.2	ISP	5
1992A	NGC 1308	s	n	15:,100:	0.3±0.3	Undetermined	6
1994D	NGC 4526	b	n	-10	0.35±0.2	Undetermined	7
1994ae	NGC 3370	b	n:	≥ 30	0.3	Upper limit	7
1995D	NGC 2962	b	n:	14, 41	0.2	Upper limit	7
1996X	NGC 5061	s	n	-7,30	0.3±0.3	Maybe?	8
1997dt	NGC 7448	s	n:	≥ 0:	?	Yes?	9
1998bu	M 96	b	n	-4,-3,-2	2.1±0.1	ISP	10
1999by	NGC 2841	s	s	-2,-1,0	0.8±0.1	Yes	11

^aSpec – Type of measurement, broadband (b) or spectropolarimetric (s).

^bSub – Strength of SN – normal(n) or subluminous (s)

^cApproximate number of days past maximum light observations were taken.

^dDetection – Whether or not this is a detection of polarization intrinsic to the SN.

References–(1) Wolstencroft & Kemp 1972; (2) Shakhovskoi 1976; (3) Shapiro & Sutherland 1982; (4) McCall et al. 1984a; (5) Hough et al. 1987; (6) Spyromilio & Bailey 1993; (7) Wang et al. 1996; (8) Wang et al. 1997b (9) Leonard et al. 2000a; (10) Hernandez et al. 2000; (11) this work

Table 3. Stars within a 5° radius of SN 1999by

Name ^a	Gl _{on} ^b °	Gl _{at} ^c °	pol ^d %	GPA ^e °	EPA ^f °	V ^g mag	SpT ^h	A _V ⁱ mag	μ ^j mag
82621	164.82	45.87	0.05	81.3	6.0	4.6	A2V	0.0	3.0
82328	165.42	45.68	0.01	11.1	115.0	3.2	F6IV	0.0	1.4
77770	169.27	41.90	0.37	79.0	175.0	7.5	B2IV	0.0	10.6
SN 1999by	166.91	44.12							

^aName — HD Name

^bGl_{on} — Galactic longitude

^cGl_{at} — Galactic latitude

^dpol — Degree of polarization

^eGPA — Position angle of the E vector in galactic coordinates

^fEPA — Position angle of the E vector in equatorial coordinates

^gV_m — Visual magnitude

^hSpT — Spectral type

ⁱA_V — Visual absorption

^jμ — Distance modulus (m — M = 5 log(r/10))

Data are from Mathewson & Ford (1978) at <http://tarantella.gsfc.nasa.gov/cgi-bin/viewer/specify.pl?file=catalog.dat&catalog=2034A>